NTNU
Norwegian University of
Science and Technology

Source Signature Estimation Based on Recordings in Deep-Towed Streamers Below the Source

Kristian Svarva Helgebostad

Petroleum Geoscience and Engineering
Submission date: June 2017
Supervisor: Martin Landrø, IGP
Co-supervisor: Vetle Vinje, CGG

Norwegian University of Science and Technology
Department of Geoscience and Petroleum

Abstract

Source-over-spread acquisition design is a recent development in marine seismic acquisition, aiming to improve imaging of the shallow subsurface. Contrary to conventional towed-streamer acquisition, source-over-spread acquisition records the direct wave below the source. We propose an inversion algorithm that takes advantage of the recordings of the direct wave in source-over-spread acquired seismic data to estimate notional source signatures for each air gun. The obtained notional source signatures from the inversion can be used to estimate directional far-field signatures, similar to the approach of notional source signatures estimated from measurements in near-field hydrophones.

The forward modeling of the algorithm is based upon a physical modeling of the air bubble created by each air gun in the source array. A damped Gauss-Newton approach is used as a local search algorithm to minimize the difference between the recorded direct wave and the modeled direct wave from the forward modeling. The inversion is first carried out for a low-frequency part of the data, before higher frequencies are included in the inversion. Typical inversion parameters are empirical damping factors for the bubble oscillations and firing time delay for each air gun. Variations in streamer depth are taken into account and a constant sea surface reflection coefficient is also estimated as a by-product of the inversion.

The algorithm is tested on shallow and deepwater data sets acquired with CGGs acquisition design called TopSeis. The notional source signatures are used in a designature flow and compared with designature results with notional source signatures from near-field hydrophone measurements. The results indicate that utilizing the direct wave in source-over-spread seismic can provide more accurate estimation of the strongest part of the bubble for deepwater data sets. To improve bubble estimation further, one may add more empirical factors to describe the oscillations of the bubble in the forward operator. It was furthermore observed that for shallow water data sets, subsurface reflections contaminated the bubble train of the direct wave. This affected the stability of the inversion, even when the water bottom reflection was included in the forward modeling.

Sammendrag

Å plassere den seismiske kilden over lyttekablene i marin innsamling av seismikk er et nytt konsept som er utviklet for å forbedre grunn avbildning av undergrunnen. I motsetning til tradisjonell tauet kabel-seismikk, vil man med dette nye innsamlingsoppsettet måle direktebølgen i lyttekablene som er plassert under kilden. Vi foreslår en inversjonsalgoritme for å estimere den effektive kildesignaturen fra hver luftkanon i kildekonfigurasjonen ved hjelp av målingene av direktebølgen under kilden. De effektive kildesignaturene kan deretter bli brukt til å estimere retningsavhengige fjernfeltssignaturer med tilsvarende tilnærming som blir brukt med effektive kildesignaturer estimert fra målinger i nærfeltshydrofoner.

Framovermodelleringen i algoritmen er basert på fysisk modellering av luftboblene fra hver luftkanon i den seismiske kilden. En dempet Gauss-Newton-tilnærming er brukt som en lokal søksalgoritme for å minimiere forskjellen mellom den målte direktebølgen og den modellerte direktebølgen fra vår framovermodellering. Vi utfører inversjonen først over en lav-frekvent del av data-settet, før høyere frekvenser er inkludert i inversjonen. Typiske inversjonsparametre i framovermodelleringen er empiriske dempningsfaktorer for boble-oscillasjonene og avfyringsforsinkelse for hver luftkanon. Variasjoner i kabel-dyp blir også tatt hensyn til og en konstant refleksjonskoeffisient for havoverflaten blir også estimert fra inversjonen.

Algoritmen er testet på datasett innsamlet i grunt og dypt vann med CGGs innsamlingsdesign kalt TopSeis. De effektive kildesignaturene er brukt i en designatur-algoritme, hvor resultatene er sammenlignet med designatur med effektive kildesignaturer fra nærfeltshydrofoner. Resultatene viser at å bruke målingene av direktebølgen i denne type datasett kan forbedre estimeringen av den sterkeste delen av boblen for datasett samlet inn på dypt vann. For å forbedre bobleestimeringen ytterligere, kan man inkludere flere empiriske faktorer for å beskrive oscillasjonene til boblene. Det ble videre observert at boblen fra direktebølgen var dekket til av refleksjoner for datasett på grunt vann. Dette påvirket stabiliteten til inversjonen, selv når havbunnsrefleksjonen ble inkludert i framovermodelleringen.

Preface

The following master's thesis in Petroleum Geophysics was submitted to the Department of Geoscience and Petroleum at the Norwegian University of Science and Technology (NTNU) 9th of June 2017. The thesis was executed in collaboration with CGG Services (Norway) AS and has been supervised by professor Martin Landrø at NTNU and co-supervised by Vetle Vinje, Principal Research Geophysicist at CGG.

The master's thesis is a continuation of Helgebostad (2016), which was a specialization project delivered at NTNU in the fall of 2016. Therefore, some of the content of Helgebostad (2016) is included here.

The thesis investigates how the recorded direct wave in source-over-spread acquisition designs can be utilized for source signature estimation, with emphasis on CGGs TopSeis acquisition design (launched September 2016). During my summer internship at CGG in 2016, Vetle Vinje suggested that working with TopSeis data could be relevant for my thesis. Professor Martin Landrø introduced me to a method I could use to estimate source signatures based on measurements of the direct wave below the source, and this formed the basis of my specialization project and following master's thesis.

I would like to acknowledge CGG Services (Norway) AS for allowing me to work with exciting technology and research. I would also like to thank Carl-Inge Nilsen, Thomas Elboth and Erik Hicks for advices and fruitful discussions. Finally, I would like to thank my supervisors, Vetle Vinje and Martin Landrø for their countless ideas and helpful feedback over the last year.

The work presented in this thesis is intended for readers with experience in acquisition and processing of marine seismic data.

Trondheim, June 9th, 2017

Kristian Svarva Helgebostad

Table of Contents

List of Tables

List of Figures

Abbreviations

AVO = Amplitude Versus Offset

FWI = Full-Waveform Inversion

NFH = Near-Field Hydrophone

OBS = Ocean-Bottom Seismic

PBR = Peak-to-Bubble Ratio

SRME = Surface-Related Multiple Elimination

SWIM = Seperated Wave-field Imaging

VDS = Variable-Depth Streamer

Chapter 1

Introduction

Recent advances in marine seismic acquisition have been made in order to overcome the lack of near-offset data in conventional towed-streamer seismic. Near-offset data from conventional towed-streamer seismic have not been commercially available until September 2016, when CGG launched TopSeis. TopSeis is a dual-vessel acquisition design that places a source vessel over a towed receiver spread, providing near offsets and also increased fold in the seismic data. Near-offset data are valuable in areas with shallow water depth and complex geology with high velocities in the shallow subsurface, for example in the Barents Sea.

With the increasing need for improved imaging of the subsurface, source signature estimation has become a key step in processing of marine seismic data. Accurate estimation of source signatures are important for designaturing of the seismic data, whereby the source signature is converted into a desired output wavelet. Beyond designature, accurate source signatures are also decisive to obtain good results in FWI, time-lapse seismic and SRME, among others. In conventional towed-streamer seismic, the source signature is usually estimated from near-field measurements in hydrophones placed close to each air gun in the air gun array. However, this approach can be inaccurate due to the complex and non-linear dynamics in the near-field. For source-over-spread acquisition designs, where the streamers are towed below the source, an alternative approach is to estimate the source signature from the measurements of the direct wave in the streamers. This method can partly overcome the challenges of using near-field measurements, and can therefore provide more accurate estimation of source signatures.

The content of this thesis is to develop and test an inversion algorithm for source signature estimation based on the recordings of the direct wave in deep-towed streamers below the array.

The forward modeling of the algorithm uses a physical modeling of the pressure output from each air gun in an air gun array to model the direct wave. A local search algorithm is used to find the model that minimizes the difference between the recorded and the modeled direct wave in the streamers. The method is tested on data sets acquired with CGGs TopSeis design, both in shallow and deep water. The obtained notional source signatures from the inversion are used in a designature flow and compared with designature results with notional source signatures estimated from measurements in near-field hydrophones.

The outline of the thesis is as follows: Chapter 2 serves as an introduction to marine seismic data acquisition, and some of the improvements that have been made over the last 10 years. The forward modeling, inversion scheme and designature theory is explained in Chapter 3. In Chapter 4, the algorithm is tested on two data sets and the results are presented. The results are further discussed in Chapter 5, before the thesis wraps up with a conclusion in Chapter 6.

Chapter 2

Marine Seismic Data Acquisition

About one third of global production of hydrocarbons is produced offshore (PlaneteEnergies, 2015), and the increasing energy demand has challenged the oil industry to explore for hydrocarbons in more challenging geological settings. The costs related to drilling offshore wells are high compared to onshore wells, and therefore, subsurface investigation prior to drilling is key to reduce exploration risks and maintain a sustainable exploration program. For this purpose, marine seismic acquisition is the most important exploration tool in the offshore oil and gas industry. A seismic source is emitting energy that is propagating down in the earth. Some of the energy is reflected from the subsurface and is recorded in seismic sensors, most commonly placed along streamers that are towed behind a vessel. The recorded data are processed to create an image of the subsurface, which is used as a tool to identify drilling prospects. The acquisition design can be tailor-made for the project, in order to accommodate for the complexity of the subsurface.

With exploration in more challenging geological settings, the need for improved imaging of the subsurface has increased. There have been many significant advances in seismic acquisition and imaging. The most recent advances aim to extend the frequency bandwidth of the seismic pulse with innovative source and streamer designs. A new recent focus area is to overcome the lack of near-offset data in towed-streamer seismic.

2.1 Marine Seismic Sources

A seismic source is defined as any device which releases energy into the earth in the form of seismic waves (Landrø and Amundsen, 2010). In marine seismic acquisition, air guns have been the most commonly used source. An air gun is a chamber of compressed air which is released into the water and creates an acoustic pulse. When the compressed air is released, an oscillating bubble is formed (described e.g. by Parkes and Hatton (2013)), as shown in Figure 2.1 from Langhammer (1994). The oscillations will be dampened because of frictional forces and will stop when the bubble dissolves or breaks the sea surface.

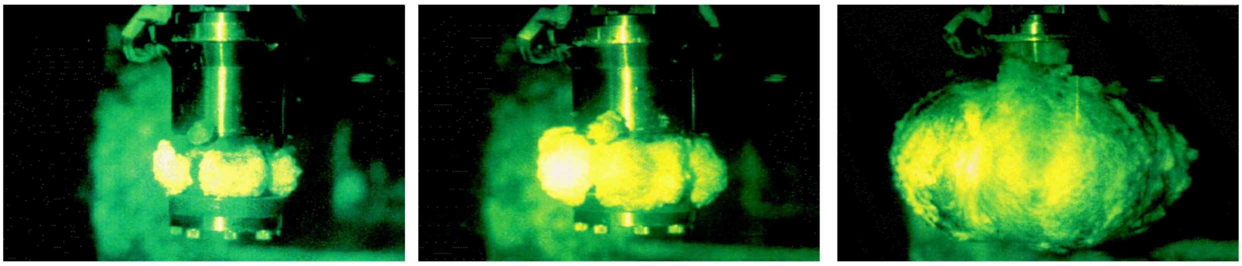

Figure 2.1: Expansion of a bubble after an air gun is fired in water (Langhammer, 1994).

The ideal signature from a single air gun is the pressure emitted from the first expansion of the bubble. However, the oscillations of the bubble create unwanted characteristics in the source signature. In order to mitigate the bubble effect in the source signature, seismic sources normally consist of several air guns with different chamber volume. The bubble effects from the air guns partly cancel out, because the bubble time period depends on the volume of the chamber.

Another unwanted effect in the source signature is the source ghost. Simultaneously as a pressure pulse is traveling downwards, another pressure pulse is traveling upwards towards the sea surface where it is reflected and inverted, before it travels downwards together with the originally downward-traveling pressure pulse. This pulse is called the source ghost and is considered to be a part of the source signature.

Figure 2.2 from Langhammer (1994) shows the source signature from a 40 cu.in. air gun, without and with the source ghost. Figure 2.2a clearly shows the effect of the oscillations from the bubble and Figure 2.2b shows the effect of the source ghost in the source signature. Modern air gun arrays are typically designed to maximize the PBR (Peak-to-Bubble Ratio), which is the

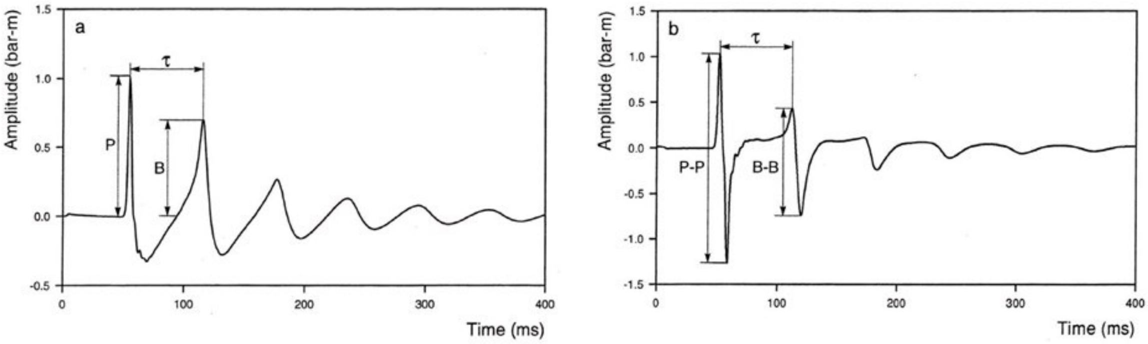

(a) Air gun signature **(b)** Air gun signature including source ghost

Figure 2.2: Air gun signatures without (left) and with (right) source ghost effect (Langhammer, 1994). τ is the bubble time period, P is the primary pressure, B is the bubble pressure, P-P is the Peak-to-Peak amplitude and B-B is the Bubble-to-Bubble amplitude.

ratio between the P-P and B-B amplitudes, as denoted in Figure 2.2b. A high PBR will provide a smooth signal spectrum which is preferred when the seismic data are processed.

The source ghost is a major challenge in marine seismic acquisition because it creates notches and depressions in the frequency spectrum of the seismic pulse which hampers the seismic resolution. In the frequency spectrum, the notches are given by,

$$f_n = n\frac{c}{2z_s\cos\theta} \qquad n = 0, 1, 2, 3, ... \tag{2.1}$$

where f_n is the frequency of the n^{th} notch, c is water velocity, z_s is the source depth and θ is the propagation direction relative to the vertical. The first ghost notch will always appear at 0 Hz, whereas the other notches depend on the source depth, propagation direction and water velocity. Figure 2.3 shows the ghost filter for source depths of 6 m and 9 m and $\theta = 0°$ (i.e. vertical propagation), where the notches occur at different frequencies. Because of the depth-dependency of the source ghosts, air gun arrays can be customized for the target of the acquisition. For example, if shallow imaging is main priority, the air gun arrays will fire at shallow depth to keep the high frequencies in the signal. In recent years, seismic companies have started to divide seismic sources into sub-sources (Parkes et al., 2011; Siliqi et al., 2013) where the sub-sources fire at different depth, with the objective of diversifying the notches in the frequency spectrum. Haavik and Landrø (2015) propose variable source depth acquisition as an improved method to attenuate the effect of the source ghost. Both dual-level sources and variable source depth acquisition aim to fill in the notches in the signal spectrum to improve the resolution of the image of the subsurface.

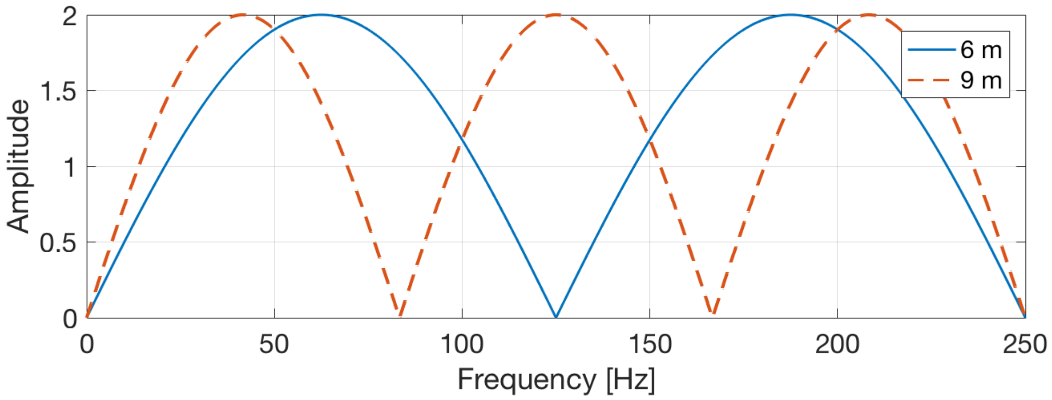

Figure 2.3: Vertical ghost filter for an air gun at 6 m (solid blue) and an air gun at 9 m (dashed red). Firing at shallower depth pushes the first non-zero notch to higher frequencies.

2.2 Broadband Streamer Technology

The benefits of acquiring marine broadband seismic have been recognized for a long time, but been difficult to achieve. Similar to the source ghost, there is a receiver ghost that is reflected off the sea-surface before it is recorded by the receivers. The receiver ghost will create notches and depressions in the signal spectrum (depending on the depth of the receiver, water velocity and propagation direction) and broadband streamer technology aims to reduce this impact, so that more low- and high-frequency signal is recorded. Low frequencies provide better penetration for deeper targets, reduce the sidelobes of the wavelet and improve inversion results (Ten Kroode et al., 2013), whereas higher frequencies results in better resolution because the wavelet is sharper. Sønneland and Berg (1985) explain how the wave-field can be separated into up- and down-going wave-fields with over/under acquisition (towing streamers simultaneously at different depth), but early attempts were unsuccessful due to poor vertical alignment control of the towed streamers. It was not before the mid 2000's that seismic companies were able to achieve over/under acquisition; with improved streamer steering technology, WesternGeco was able to successfully align the streamers (Hill et al., 2006). However, the true break-through for broadband streamer technology is often credited Petroleum-Geo Services with their GeoStreamer, launched in 2007.

2.2.1 Dual-Sensor Technology

GeoStreamer was presented at the EAGE meeting in London, 2007 (Tenghamn et al., 2007). Geophysicists have known for long that by recording vertical particle velocity in addition to pressure, one could be able to separate the wave-field into up- and down-going wave-fields and cancel out the receiver ghost (Schneider and Backus, 1964; Claerbout, 1986). Many attempts had earlier been made to implement particle velocity sensors in the streamers, but the main problem related to these attempts was that the readings from the particle velocity sensors were contaminated by strum noise (mechanical vibrations propagating along the streamer). However, with PGS' modern particle motion sensors, the strum noise is restricted to the low-frequency end of the particle velocity data. PGS found that after a low-cut filter to eliminate the part of the spectrum that contained strum noise, they could recalculate this part of the velocity sensor's spectrum from the same portion of the hydrophone's spectrum.

Tenghamn et al. (2007) show that the hydrophone signal (in the frequency-domain), H, can be expressed as,

$$H = (1 - z^n)\beta \tag{2.2}$$

where $z = e^{-2\pi j f}$ is a frequency-domain time-delay operator (f is frequency and j the unit imaginary number), n is the ghost reflection delay time and β is the up-going wave-field. In the same manner, the velocity motion's spectrum, V, can be expressed as,

$$V = (1 + z^n)\beta \tag{2.3}$$

Thus, the velocity motion's spectrum can be calculated from the hydrophone's spectrum by combining Equation 2.2 and 2.3,

$$V = \frac{(1 + z^n)}{(1 - z^n)} H \tag{2.4}$$

Notice that the particle velocity's spectrum cannot be calculated from Equation 2.4 where $z^n = 1$, because this is where the ghost notches occur in the hydrophone spectrum. This puts a constraint on how deep the streamers can be towed, as the calculation of the particle velocity spectrum will be poor if the hydrophone spectrum has ghost notches in this frequency window. CGG managed to overcome this challenge with their variable-depth streamer solution.

2.2.2 Variable-Depth Streamer

Streamers have historically been towed at a constant depth behind the vessel, which results in notches and depressions of nearly constant frequencies in the frequency spectrum of the signal. CGG changed this rule of thinking, when they launched BroadSeis in 2010 (Soubaras and Dowle, 2010; Amundsen and Landrø, 2016). Their variable-depth streamers exploit that the ghost notches vary with receiver depth. This can be illustrated by considering vertically traveling waves. The ghost operator in the frequency-domain can be described as,

$$G(f) = 1 - e^{-2\pi j f t} \tag{2.5}$$

where j is the unit imaginary number, f is the frequency and t is the receiver ghost delay. If zero-offset data from N receivers are stacked, the residual receiver ghost filter will be given by,

$$G(f) = \frac{1}{N}\sum_{i=1}^{N} 1 - e^{-2\pi j f t_i} \tag{2.6}$$

where t_i is the receiver ghost delay for receiver i. For streamers that are towed at constant depth, the time delay will be the same at all receiver positions for zero-offset data. However, for variable-depth streamers, the time delay will vary along the cable, and thus, the receiver ghost will be stacked out. This is shown in Figure 2.4, where the receiver ghost filter for a variable-depth streamer is compared to receiver ghost filters for streamers towed at a constant depth of 7.5 and 15 m. An alternative to the variable-depth streamer profile in Figure 2.4 is to tow the streamers slanted, also with the objective of varying the receiver ghost delays along the streamer (Ray and Moore, 1982; Moldoveanu et al., 2012).

The figure illustrates the concept of variable-depth streamer acquisition; whereas conventional streamers are towed at shallow depth, causing low- and high-frequency signal to be attenuated, variable-depth streamers improve the low- and high-end frequency content by diversifying the notches. Combined with deghosting in the seismic processing, variable-depth streamer data results high-quality final images with sharp and clean wavelets. However, as for conventional streamer seismic (including broadband-solutions), variable-depth streamer solutions suffer from lack of near-offset data.

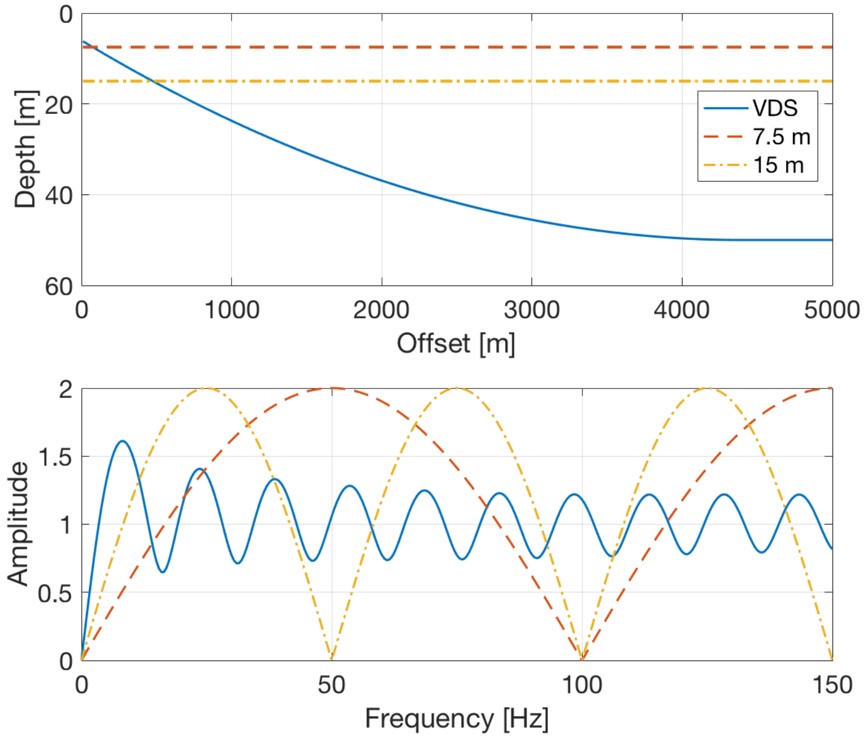

Figure 2.4: Streamer depth as a function of offset (top) for variable-depth streamer (solid blue), streamer at 7.5 m (dashed red) and 15 m (dashdotted yellow) and corresponding frequency spectrum (bottom). The variable-depth streamer profile diversifies the notches, so zero-amplitude notches are not present in the frequency spectrum.

2.3 Acquisition From Deep-Towed Streamers Below the Source

The most recent advance is to acquire seismic data from deep-towed streamers below the source, with the objective to overcome the lack of near-offset data in conventional towed-streamer seismic. Due to the drive for increased efficiency in acquisition of seismic data, the size of seismic vessels and number of streamers towed behind the vessel have increased. As a result of this, the gap between the source and first receivers has increased, and imaging of shallow reflectors with traditional reflection seismology has not been able to meet industry's expectations. Alternative imaging technologies have been suggested to overcome this problem, for example PGS' SWIM technology (Lu et al., 2015). However, true near-offset data from conventional towed-streamer seismic has not been commercially available until August 2016, when CGG launched TopSeis (Vinje et al., 2017). TopSeis is a dual-vessel design, where a source is placed above deep-towed streamers, as illustrated in Figure 2.5. Whereas broadband solutions have designed surveys to extend the frequency bandwidth of the signal, source-over-spread-solutions are designed to overcome the lack of near-offset data in conventional towed-streamer seismic. The improvement in shallow imaging that TopSeis provides is evident in Figure 2.6, where the yellow arrows highlight some of the geologic features that are not successfully imaged with conventional seismic data.

The innovative acquisition design of TopSeis offers the opportunity to utilize the direct wave recorded in the deep-towed streamers below the source (shown in Figure 2.7) for source signature estimation. Landrø (2000) discusses the need for accurate source signature estimation to benefit recent developments in the industry; FWI, time-lapse surveys, OBS and SRME (among others), which require detailed knowledge about the source signature. Today, a common method for source signature estimation is to use near-field measurements, based on Ziolkowski et al. (1982). The basic idea of Ziolkowski et al. (1982) is to remove the effect of the neighbouring sources and their ghosts on each near-field measurement to obtain effective point sources. However, Landrø et al. (1991) show that this approach can be unstable for dense air gun arrays, mainly due to non-linear dynamics in the near-field. The reasons for the non-linear dynamics have been widely discussed in recent years. Hampson (2017) suggest that linear models are not likely to be valid on the source-side, where the strains are orders of magnitude higher than on the receiver-side. Ghost cavitation, whereby the ghosted energy can produce absolute pressures of zero or less, can also occur in the near-field (Landrø et al., 2011). Additionally, for example

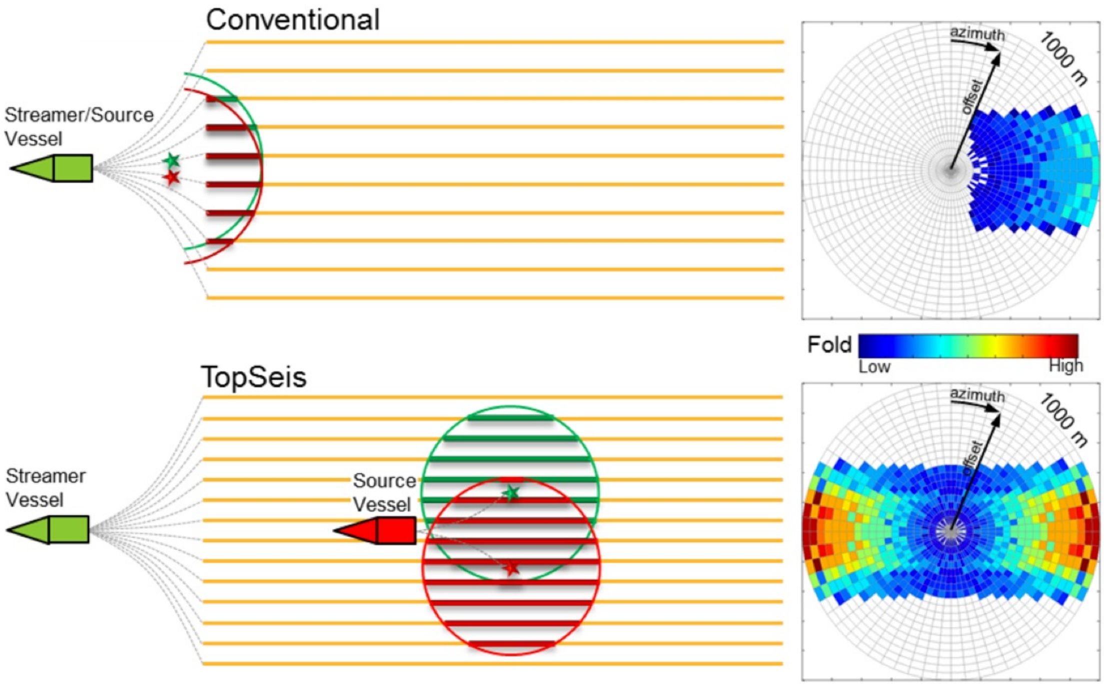

Figure 2.5: Conventional acquisition (top) and source-over-spread (TopSeis) acquisition (bottom) to the left, with corresponding rose plots to the right. Note the increased fold, near-offset and split-spread TopSeis provides. Figure courtesy of CGG.

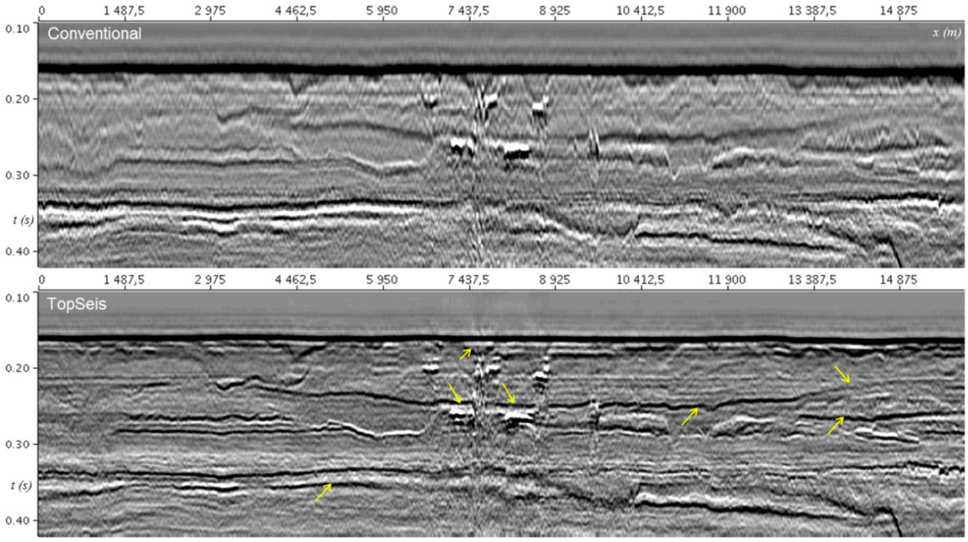

Figure 2.6: Migrated images in the shallow subsurface with conventional data (top) and TopSeis data (bottom) from the Frigg-Gamma field in the North Sea. Vertical axis is time (s) and horizontal axis is offset (m). TopSeis provides improvement in shallow imaging, especially evident where highlighted by yellow arrows.

leakage of air from the air gun chambers can complicate the physics further. The non-linear dynamics in the near-field make it difficult to remove the effect of neighbouring sources and the source ghosts from each near-field measurement. However, an alternative approach that partly overcomes the challenges with near-field measurements is to use mid-field measurements where the dynamics are more linear. Landrø and Sollie (1992) suggested to record the wave-field in a mini-streamer below the source to determine the source signature more accurately and similar methods has been proposed for OBS data. Source-over-spread acquisition design opens the door for far-field signature estimation from mid-field measurements in the towed-streamers below the source.

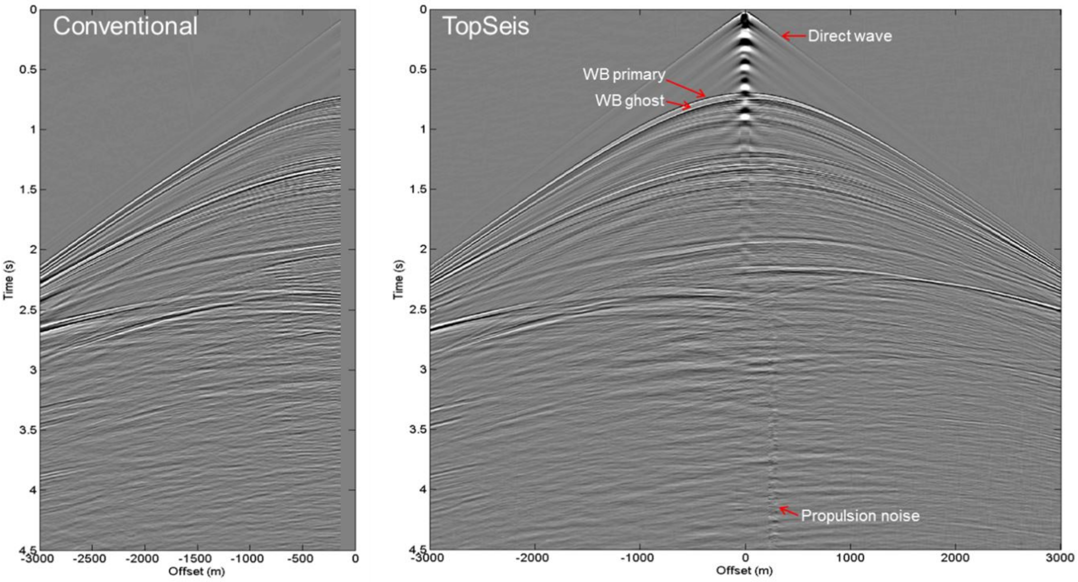

Figure 2.7: Conventional (left) and TopSeis (right) shot gathers from the same location plotted on the same scale. Vertical axis is time (s) and horizontal axis is offset (m). The shot-gather from TopSeis is split-spread with near-offset data, which is not acquired with the conventional acquisition design. The measurements of the direct wave at near offsets in TopSeis data can be utilized for source signature estimation. Figure courtesy of CGG.

Chapter 3

Theory

3.1 Fundamentals of Geophysical Inverse Methods

Geophysicists have for long recognized the need for inverting their data; to find a model that recreates the recorded geophysical data (see e.g. Backus and Gilbert (1967, 1968, 1970)). However, limited computational power has restricted the complexity of the models that can be recovered. With considerable advances in computational power, the usefulness of inversion in geophysics has increased. The data that are acquired in a geophysical survey can be denoted $\vec{d}^{obs}$, and can be split into two parts; the true data, that arise from the unknown model, and additive noise. This can be described by the equation,

$$\vec{d}^{obs} = F[\vec{m}] + \vec{n} \tag{3.1}$$

where $\vec{m}$ is the model, $\vec{n}$ is noise and F is the forward operator that incorporates details of the survey design and the relevant physical equations. The goal of the inversion is to recover the model that minimizes the difference between the observed data and the synthetic data computed with the forward operator. The inversion algorithm can be split into two parts; the forward problem; to model synthetic data from a known model, and the inverse problem; to recover the model that best fits the observed data. The two following sections will explain the theory behind the forward operator and the inversion scheme used in this thesis.

3.2 The Forward Operator: Modeling the Direct Wave

The forward operator is used to compute the synthetic data that arise from a set of sources and receivers when a model is known. Oldenburg and Li (2005) illustrate this with an example, shown in Figure 3.1. Here, the source is the earth's main magnetic field $\vec{B}_0$, the model is the 3D distribution of magnetic susceptibility and the data are the total-field anomaly. The operator $F[\vec{m}]$ computes the data that will arise from the model.

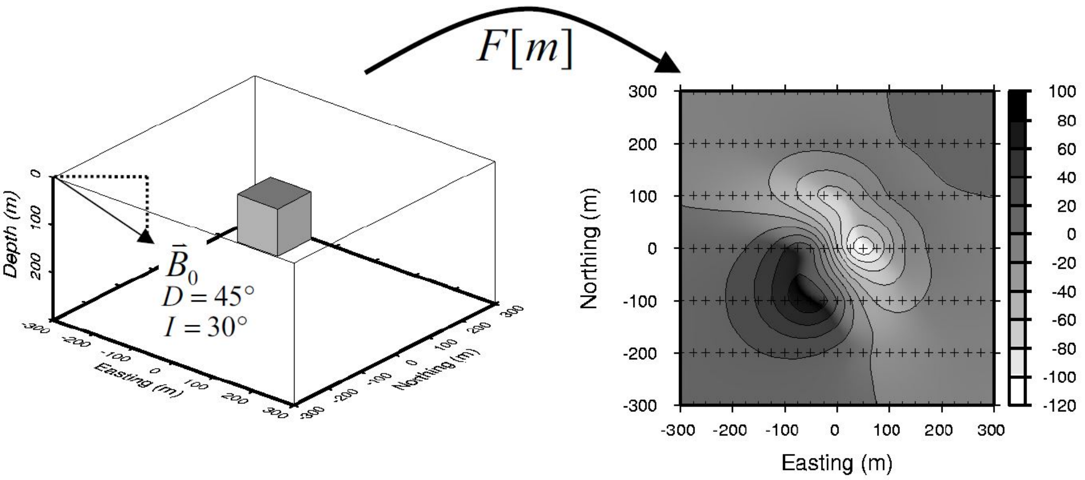

Figure 3.1: Example of the forward operator. The earth's main magnetic field $\vec{B}_0$ is the source, the model is the 3D distribution of magnetic susceptibility (left) and the data are the total-field anomaly (right) (Oldenburg and Li, 2005).

In our algorithm, the forward operator is the modeling of the far-field pressure at each receiver position as a function of time caused by the oscillating bubbles created by each air gun in an air gun array. Many studies have tried to describe the collapse time of a spherical cavity (Rayleigh, 1917; Herring, 1941; Kirkwood and Bethe, 1942; Gilmore, 1952; Keller and Kolodner, 1956; Flynn, 1964), with different assumptions. Johnson (1994) shows that for a spherical bubble in an infinite volume of water at hydrostatic pressure, p_0, the bubble motion approximately obeys,

$$\ddot{R} = \frac{p - p_\infty}{R\rho} - \frac{3}{2R}\dot{R}^2 + \frac{1}{\rho c}\dot{p} \tag{3.2}$$

where R is the bubble radius as a function of time, dot denotes the time derivative of the function, p is the acoustic pressure, p_∞ the hydrostatic pressure at the depth of the bubble center, and ρ and c are the density and velocity of the water, respectively. In our forward operator, we modify the Johnson-equation,

$$\ddot{R} = \frac{p - p_\infty}{R\rho} - \frac{3}{2R}\dot{R}^2 + \gamma\frac{1}{\rho c}\dot{p} + \alpha\frac{\dot{R}}{R} + \beta(t)\frac{\dot{R}^2}{R} \tag{3.3}$$

where γ is a fixed constant, introduced by Johnson (1994) to fit measurements and α and $\beta(t)$ are empirical factors that control the damping of the bubble and the bubble time period, respectively, inspired by Landrø and Sollie (1992). To take into account that the bubble time period between each oscillation can vary due to interaction between the bubbles, $\beta(t)$ is a time-variant factor, given by $\beta(t) = \beta_0 + \beta_1 t$. A solution of the modified Johnson-equation describe the radius of the bubble as a function of time. The pressure at the bubble wall can then be described by,

$$p(R) = p_0\left(\frac{R_0}{R}\right)^{3\lambda} \tag{3.4}$$

where p_0 and R_0 are the initial pressure and radius of the air bubble, R is the radius of the cavity as a function of time and λ is a gas constant. λ can for example be set to $\lambda = 1$, assuming isothermal bubble expansion, or $\lambda = 1.4$ for adiabatic bubble expansion. We have set $\lambda = 1.13$, similar to the value used e.g. by Ziolkowski (1970).

If the equations above are used to describe the air bubble created by an air gun, we need to assume that the time it takes to empty the air chamber is infinitely short. This is not a valid assumption, and the primary peak from the modeling will be too strong compared to the amplitude from the bubble oscillations that follows. Landrø and Sollie (1992) describe the actual transfer of air from the air chamber in their modeling. We solve this issue by scaling the primary peak, so that the amplitude of the primary peak is reasonable compared to the amplitude of the bubble oscillations.

The pressure field at a far-field point from the bubble center, created by a single oscillating air bubble, was derived by Gilmore (1952), and can be written in the form,

$$p - p_\infty = \rho_\infty\frac{R}{r}(H + \frac{\dot{R}^2}{2}) \tag{3.5}$$

where r is the distance between the bubble centre and the far-field point and H is the enthalpy at the bubble wall. Higher order terms of $\frac{1}{r}$ are neglected, because they will not be significant in the far-field. The enthalpy at the bubble wall is often evaluated by the Tait-equation (Tait, 1888), but assuming that the density of the water is independent of pressure, H can be approximated to be,

$$H \approx \frac{p - p_\infty}{\rho} \tag{3.6}$$

The far-field pressure from a 150 cu.in air gun with 139 bar chamber pressure, fired at 6 m, is shown in Figure 3.2 and illustrates the effect of the α and β-parameters. Increasing the value of α corresponds to more damping of the bubble, while decreasing the value of β_0 (β_1 is set to zero) corresponds to increasing the bubble time period.

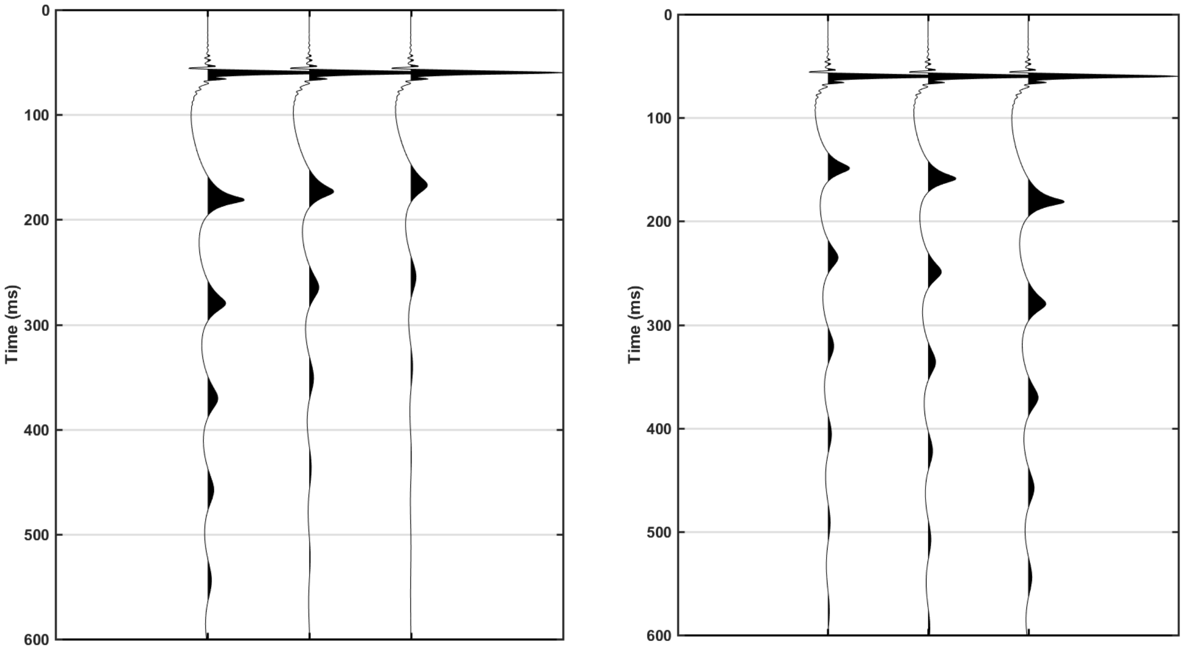

Figure 3.2: Left: Increasing α from left to right. Higher values of α yields more damping of the bubble. Right: Decreasing β_0 from left to right. Lower values of β_0 yields larger bubble time periods.

Ziolkowski et al. (1982) wrote a landmark paper on source signature estimation, where they present theory to estimate source signatures based on near-field measurements. They define the term notional source signature (notional), which is a hypothetical isotropic point source signature representing an individual gun in the source array, but taking into account the bubble interactions that occur when all of the individual air guns in the source array fire together (Davidson and Poole, 2015). For our algorithm, the interaction effects are included by introducing the empirical factors α and β, which are meant to take the interaction between the bubbles into account. This is similar to the approach of Landrø and Sollie (1992).

As the notional source signatures include interaction effects, the acoustic pressure at a far-field point can be found by superposing the notional source signatures and adding the effect of the source ghost,

$$p(t) = \sum_{i=1}^{N} \left[\frac{1}{r_i} s_i(t - \tau_i - \frac{r_i}{c}) + \eta \frac{1}{r_i^g} s_i(t - \tau_i - \frac{r_i^g}{c}) \right] \tag{3.7}$$

where N is the number of air guns, s_i and τ_i are the notional source signature and firing time delay for air gun i, c is the water velocity, η the sea surface reflection coefficient, and r_i and r_i^g the distance and ghost distance between air gun i and the far-field point, respectively.

A receiver that is used in seismic acquisition is an array of hydrophones, usually 12.5 m long, where the registered pressure at the receiver is the average of the measured pressure at each hydrophone. Because the hydrophones have slightly different positions on the streamer, the recorded wavelet will be different than if the receiver was a point receiver. This effect is called the receiver side array effect, and should be taken into account when source signatures are estimated from the direct wave, as for example Davidson and Poole (2015) do. Then, the recorded pressure from a hydrophone can be described by the equation,

$$p(t) = \frac{1}{M} \sum_{k=1}^{M} \sum_{i=1}^{N} \left[\frac{1}{r_{i,k}} s_i(t - \tau_i - \frac{r_{i,k}}{c}) + \eta \frac{1}{r_{i,k}^g} s_i(t - \tau_i - \frac{r_{i,k}^g}{c}) \right] \tag{3.8}$$

where M is the number of hydrophones for a receiver and $r_{i,k}$ and $r_{i,k}^g$ are the distance and ghost distance between air gun i and hydrophone k.

There will be significant errors if the calculation of the pressure response in Equation 3.8 is calculated in the discrete time-domain. The reason for this is that the time delay from each source to each sensor is unlikely to be equivalent to an integer number of samples. This problem can be overcome by carrying the calculation out in the frequency-domain, where the phase shifts due to the time delays will be calculated exactly. This can be described by the Fourier transform of Equation 3.8,

$$p(\omega) = \frac{1}{M} \sum_{k=1}^{M} \sum_{i=1}^{N} \left[\frac{1}{r_{i,k}} s_i(\omega) e^{-j\omega t_{i,k}} + \eta \frac{1}{r_{i,k}^g} s_i(\omega) e^{-j\omega t_{i,k}^g} \right] \tag{3.9}$$

where $t_{i,k} = \frac{r_{i,k}}{c} + \tau_i$ and $t_{i,k}^g = \frac{r_{i,k}^g}{c} + \tau_i$, ω is the angular frequency and j is the unit imaginary number. By using the described forward modeling in this section, we can model the pressure response at any receiver position for an arbitrary source configuration. As an example of the forward modeling, the pressure response at a streamer 100 meter below a three-string BroadSource (a dual level CGG source configuration) is shown in Figure 3.3. The streamer is 200 meter long, with receiver spacing of 12.5 meters. Because of the nature of the dual-level source configuration, the source ghost is de-focused in the near-offset traces.

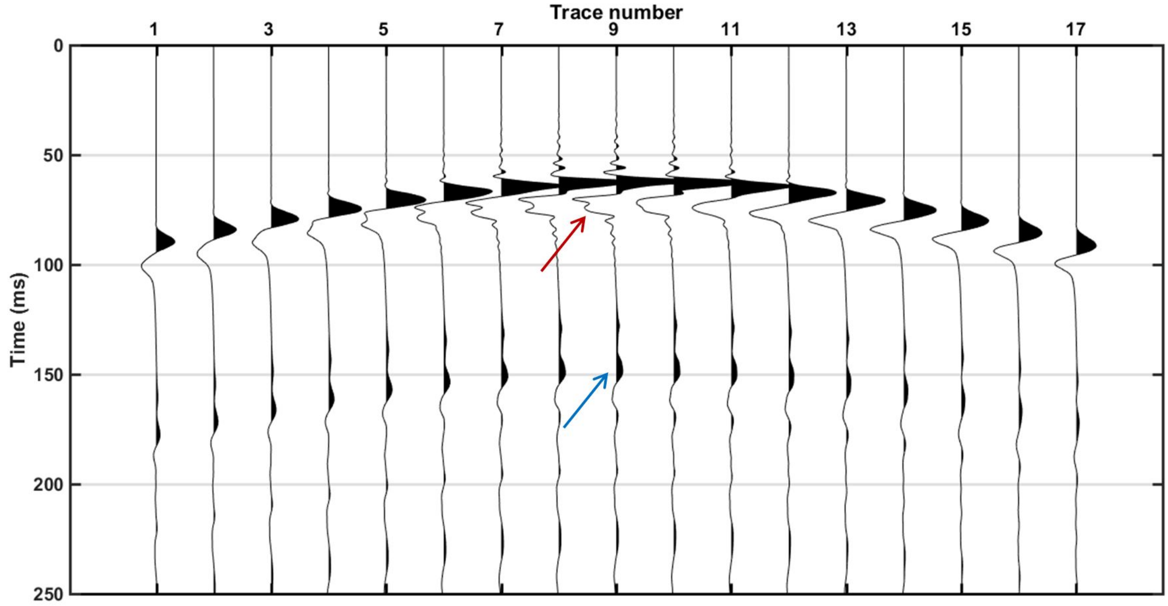

Figure 3.3: Modeled direct wave at a streamer 100 m below the source. The source ghost (highlighted by the upper arrow) is de-focused because a dual-level source has been used in the modeling. The bubble from the direct wave is highlighted by the lower arrow.

3.2.1 Extending the Forward Operator to Include the Water Bottom Reflection

When data are acquired in deep water, the water bottom reflection does not interfer with the direct wave to a significant degree. However, in shallow water, the water bottom reflection can cause problems in algorithms that try to extract information from the direct wave. To mitigate the impact of the water bottom reflection, many algorithms include this reflection in the forward modeling. This has for example been suggested when notional source signatures are estimated from near-field hydrophone measurements in shallow water (Hopperstad and Laws, 2006).

Similar to other algorithms that extract information from the direct wave, our inversion algorithm will be sensitive to reflections in shallow water. Therefore, we suggest to include the water bottom reflection and its ghosts in the forward modeling in such cases. The goal of this approach is not to model these events perfectly, as they will depend on several parameters, such as an angle-dependent reflection coefficient for the water bottom and variations in sea depth along the sail line, but to include a first-order, simplistic approximation of the water bottom reflection and its ghosts. In the modeling of the reflections from water bottom, we therefore assume that the reflection coefficient is not dependent on angle of incidence, and that the sea depth is the same for the ray paths to each receiver (i.e. the water bottom is flat). In reality, also reflections from the shallow subsurface will contaminate the bubble train of the direct wave, but we assume that these reflections are negligible compared to the direct wave.

The forward modeling from Equation 3.9 can therefore be corrected to also model the water bottom reflection (and the associated ghosts) by adding the four latter terms in Equation 3.10.

$$\begin{aligned} p(\omega) = \frac{1}{M}\sum_{k=1}^{M}\sum_{i=1}^{N}\Big[& \frac{1}{r_{i,k}} s_i(\omega) e^{-j\omega t_{i,k}} + \eta \frac{1}{r^{g}_{i,k}} s_i(\omega) e^{-j\omega t^{g}_{i,k}} + \kappa \frac{1}{r^{wb}_{i,k}} s_i(\omega) e^{-j\omega t^{wb}_{i,k}} \\ & + \kappa\eta \frac{1}{r^{wb_{sg}}_{i,k}} s_i(\omega) e^{-j\omega t^{wb_{sg}}_{i,k}} + \kappa\eta \frac{1}{r^{wb_{rg}}_{i,k}} s_i(\omega) e^{-j\omega t^{wb_{rg}}_{i,k}} + \kappa\eta^2 \frac{1}{r^{wb_{srg}}_{i,k}} s_i(\omega) e^{-j\omega t^{wb_{srg}}_{i,k}} \Big] \end{aligned} \tag{3.10}$$

where κ is the angle-independent water bottom reflection coefficient, r^{wb}, $r^{wb_{sg}}$, $r^{wb_{rg}}$, $r^{wb_{srg}}$ and t^{wb}, $t^{wb_{sg}}$, $t^{wb_{rg}}$, $t^{wb_{srg}}$ are the travel distance and travel time (adjusted for firing time delay) for the primary reflection, source ghost, receiver ghost and source receiver ghost from the water bottom, respectively.

3.3 Inverse Problem: Recovering the Unknown Model

The goal of the inverse problem is to recover a model that explains the observed data. Oldenburg and Li (2005) exemplify this with a model of the earth's magnetic susceptibility, shown in Figure 3.4. While the model was known in Figure 3.1, the problem is now to recover the magnetic susceptibility model from the noise contaminated total field anomaly data measured at the surface.

In our algorithm, we aim to find a set of notional source signatures that minimizes the difference between the modeled direct wave from the forward modeling and the observed data.

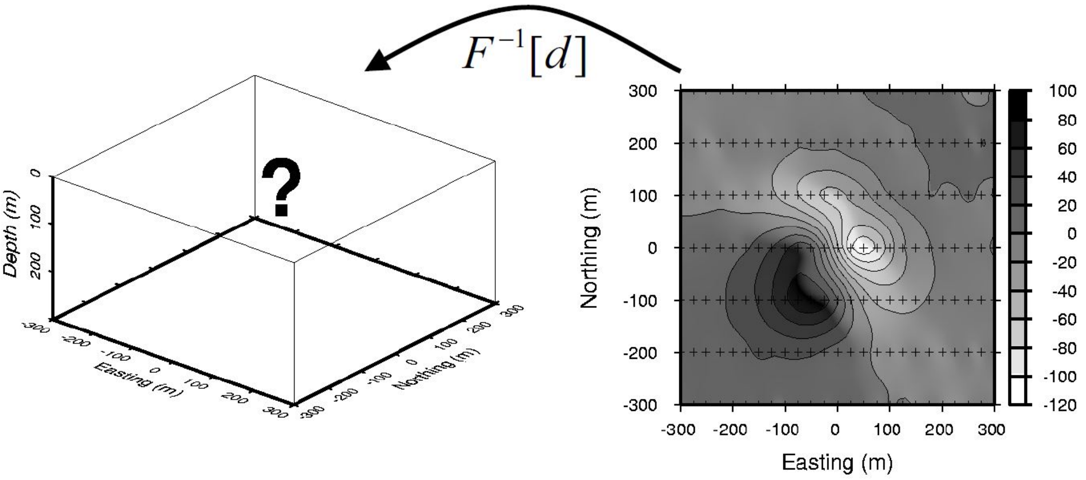

Figure 3.4: Illustration of the goal of an inverse problem. The objective is to recover the earth's magnetic susceptibility (left) from the noise contaminated total field anomaly data measured at the surface (right). (Oldenburg and Li, 2005)

This can be formulated by minimizing a data misfit function, ϕ_d,

$$\phi_d = \sum_{i}^{N_r}\sum_{j}^{N_t}(s(\vec{x}_i, t_j) - s^{obs}(\vec{x}_i, t_j))^2 \tag{3.11}$$

where $s(x_i, t_j)$ and $s^{obs}(x_i, t_j)$ are the modeled and measured pressure at a time t_j and receiver position $\vec{x}_i$, respectively, N_r is the number of receivers and N_t is the number of time samples.

The forward operator in our algorithm is non-linear, which means that the relationship in Equation 3.12 does not hold.

$$F[c_1 m_1 + c_2 m_2] = c_1 F[m_1] + c_2 F[m_2] \tag{3.12}$$

where c_1 and c_2 are coefficients and m_1 and m_2 are models. Non-linear inversion problems can be solved iteratively with a local search algorithm. Local search algorithms are cost-efficient, but they only find the global minimum if the error function is smooth or if the starting model is sufficiently close to the global minimum. If the error function is complex, global search algorithms (e.g. simulated annealing or Monte Carlo) can give better results because they will not be trapped in local minima. However, global search algorithms are computationally intensive as the number of numerical operations will increase.

We use a damped Gauss-Newton approach, which is a local search algorithm, inspired by Landrø and Sollie (1992). Objective functions for local search algorithms are typically generalized. This means that there are constraints on how well the observed data should be fit and how prior information about the model should be used (discussed for example by Tarantola (2005)). Then, the aim is to minimize the objective function,

$$\phi = \phi_d + \beta \phi_m \tag{3.13}$$

where β is a regularization parameter (Tikhonov et al., 1977). In our inversion scheme, we aim to fit the recorded data as well as possible. Therefore, β is set to zero, and the objective function is reduced to only include the data misfit function ϕ_d (Equation 3.11). The function's value at a perturbed value $m^n + \delta m$ can be found using Taylor Series,

$$\phi(m^{(n)} + \delta m) = \phi(m^{(n)}) + g^T \delta m + \frac{1}{2} \delta m^T H \delta m + \ldots \tag{3.14}$$

where g is the gradient and H is the Hessian evaluated in $m^{(n)}$. The components of the gradient and Hessian are given as,

$$g_i = \frac{\delta \phi(m)}{\delta m_i} \qquad H_{ij} = \frac{\delta^2 \phi(m)}{\delta m_i \delta m_j} \tag{3.15}$$

We want to find a perturbation so that ϕ is minimized. Neglecting higher order terms and taking the derivative of Equation 3.14 with respect to δm and setting the resultant equal to zero yields,

$$H \Delta m = -g \tag{3.16}$$

H can be approximated as $H \approx J^T J$ and $g = J^T \Delta d$, where Δd is the residual data vector. The Jacobian matrix is given by $J_{ij} = \frac{\delta d_i}{\delta m_j}$ where i runs over the data space and j over the model space. J is calculated with a finite difference approximation. With these approximations, Equation 3.16 can be written as,

$$J^T J \Delta m = -J^T \Delta d \tag{3.17}$$

which is a form of the Gauss-Newton equation. Marquardt-Levenberg (Marquardt, 1963) replaced the Gauss-Newton equation with a damped version,

$$(J^T J + \lambda I)\Delta m = -J^T \Delta d \tag{3.18}$$

where λ restricts the size of a perturbation so that the quadratic Taylor expansion is valid. λ can be scaled iteration-wise, where high values of λ result in steps in the steepest-descent direction and low values of λ results in an algorithm closer to Gauss-Newton (Equation 3.17). For the implemented inversion algorithm, λ is unchanged for the first iteration of the inversion loop and for subsequent iterations scaled by the relative error between the real and modeled data.

To avoid numerical instabilities related to the large magnitude differences between the model parameters, the Hessian matrix and the gradient vector are scaled (similar to e.g. Helgesen and Landrø (1993)),

$$\widetilde{H}_{ij} = \frac{H_{ij}}{\sqrt{H_{ii}H_{jj}}} \tag{3.19}$$

$$\widetilde{g}_i = \frac{g_i}{\sqrt{H_{ii}}} \tag{3.20}$$

With the scaling introduced, the aim is to solve Equation 3.21 and 3.22 iteratively until a convergence criterion is met.

$$\Delta\widetilde{m} = (\widetilde{H} + \lambda I)^{-1}\widetilde{g} \tag{3.21}$$

$$m^{n+1} = m^n + \Delta m \tag{3.22}$$

where $\Delta m = \frac{\Delta\widetilde{m}}{\sqrt{H_{ii}}}$. A typical convergence criterion is that the change in relative error between two iterations is less than a pre-defined threshold.

The unknown model parameters in the inversion scheme are α, β_0, β_1 and firing time delay for each air gun, parameters that describe the streamer depths, sea surface reflection coefficient and a global scaling factor. In the case where the water bottom reflection (and the associated ghosts) are included in the forward modeling, an angle-independent water bottom reflection and the (assumed constant) water depth are also unknown model parameters. The depth of the receivers are needed in the forward modeling, but they are not known exactly in practice.

Therefore, we treat them as unknowns in the inversion scheme. The receivers are placed along a streamer, so we describe the streamer depth and shape as a limited Fourier series with a gradient term, as in Equation 3.23. This is more realistic and cost-efficient than treating the individual receiver depths as unknown model parameters.

$$z(x) = z_r + cx + \sum_{n=1}^{K} \left[a_n cos\left(\frac{2\pi nx}{L}\right) + b_n sin\left(\frac{2\pi nx}{L}\right)\right] \tag{3.23}$$

where L is the streamer length, a_n and b_n are Fourier coefficients, c is a gradient term and K is the number of Fourier coefficients. This function will express the receiver depths reasonably well, without using too many unknown model parameters to describe them. The sea surface reflection coefficient is often assumed to be -1, even though it in reality is angle- and frequency-dependent (Orji et al., 2013). We assume that the sea surface reflection coefficient is a constant, but accept that it can deviate from the ideal value of -1, so it is therefore treated as an unknown parameter.

When the inversion is carried out for the full bandwidth of the data, the model parameters that control the primary pulse of the direct wave will dominate (e.g. firing time delay and streamer depth). Therefore, the inversion is first carried out for a low-frequency part of the data where only the α, β_0, β_1, the global scaling factor and sea surface reflection coefficient are inverted for (and water depth and water bottom reflection coefficient if water bottom reflection is included in the forward modeling). Then, the estimated parameters from the low-frequency part of the data are used as initial parameters when the inversion is carried out for the full bandwidth of the data, where also the streamer shape and firing time delays are inverted for. This approach has similarities to what is done in full waveform inversion, where Bunks et al. (1995) propose multiscale seismic waveform inversion because the objective function has less local minima for long wavelengths.

3.4 Source Designature

The objective of the source designature process is to convert the raw seismic wavelet that is recorded from a reflection into a desired wavelet, for example a zero-phase wavelet, as illustrated in Figure 3.5. To be able to shape the seismic wavelet successfully, the source signature is assumed to be known. The source signature can either be modeled, or extrapolated from notional source signatures estimated from for example from NFH-measurements or the inversion presented in this thesis. By adding the notional source signatures, adjusting for the difference in travel time from each air gun and adding the effect of the source ghost, we can estimate the directional far-field signature that is required in the designature process.

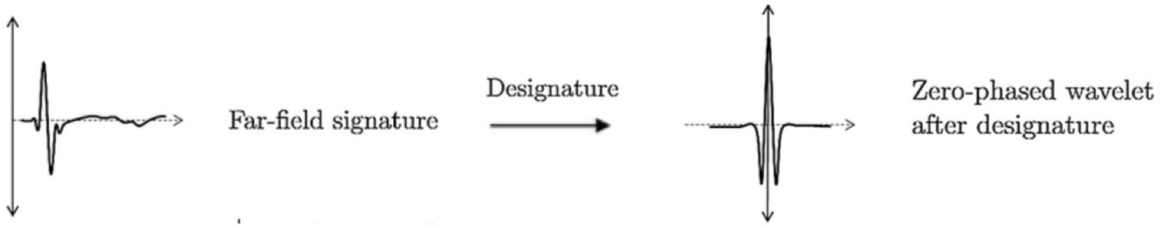

Figure 3.5: Conceptual illustration of designature. After a designature, the wavelet is shaped from the far-field signature to a zero-phase wavelet.

If the estimated signature recorded from a reflection at a receiver is denoted by $p(\omega)$, where ω is the angular frequency, there is a filter, $f(\omega)$, that can be applied to $p(\omega)$, so that $p(\omega)$ is shaped into a desired zero-phase wavelet, $G(\omega)$,

$$f(\omega)p(\omega) = G(\omega) \tag{3.24}$$

This means that the filter is given by,

$$f(\omega) = \frac{G(\omega)}{p(\omega)} \tag{3.25}$$

Then, the filter, $f(\omega)$, can be applied to the data to shape the reflections into the desired zero-phase wavelets. This is straight forward as long as the directional far-field signature is accurately estimated and we keep away from the notches in $p(\omega)$. To avoid instabilities in cases where $p(\omega)$ has notches, the filter is often regularized.

$$f(\omega) = \frac{G(\omega)}{p(\omega) + \epsilon} \tag{3.26}$$

where ϵ is a regularization parameter which limits the boosting of the frequencies in the notch regions. Another assumption of this designature approach is that the departing angle is known, which it in general is not. Recent work has been done to develop more robust designature algorithms to cope with these challenges. For example, CGGs designature tool is carried out in the τ-p_x-p_y domain, where an sparse inversion approach is applied to designature the data. This designature tool also tries to deal with the challenge of not knowing the departing angle (Poole et al., 2015).

Chapter 4

Results

By March 2017, CGG had performed two field trials with the TopSeis acquisition design. One test offshore Gabon and one over the Frigg-Gamma field in the North Sea. The inversion algorithm has been tested for both cases; on a shot in deep water from the Gabon field test and a shot in shallow water from the Frigg-Gamma field test.

Section 4.1 provides general information about the source configuration and instrument filter that were used during acquisition for the two tests. In Section 4.2, we explain why overloading of the receivers occurs and discuss the problems that arise from it. In Section 4.3 and 4.4, we present results from the deep and shallow water data sets, respectively. For both data sets, we focus on three main points:

1. Data preparation: Which receivers that are used in the inversion and what corrections that have been applied to the data before the inversion.

2. Inversion results: We focus on how the estimated model recreates the real data, present the estimated model parameters, compare estimated notional source signatures from NFH-measurements with the inversion approach and compare estimated far-field signatures from the notional source signatures with far-field signatures from Nucleus.

3. Source designature results: We designature the shallow and deepwater data with notional source signatures from the inversion and NFH-measurements and compare the results.

The estimated far-field signature will be given more attention for the deepwater case, where there is a clean recording of the direct wave, uncontaminated by reflections. Notional source signatures will further on partly be referred to as notionals.

4.1 Data Acquisition

4.1.1 Source Configuration

A BroadSource source configuration (shown in Figure 4.1) was used in both field tests. This is a dual-level source, designed to diversify the notches from the source ghost. As can be seen from the figure, many of the air guns are put together in clusters of two air guns, which is a popular way to improve the signal created by an air-gun array. Many studies have investigated the effect of the interaction between the air bubbles when the air guns fired in close proximity to each other (Strandenes and Vaage, 1992; Barker and Landrø, 2012) and it is clear that the air bubbles created by each air gun do not behave as two single air bubbles.

In our algorithm, we treat clusters of two air guns as a single air gun with a volume that is equal to the sum of the volume of the two air guns in the cluster. This is done for simplicity, as it is complicated to model the physics of clustered air guns, and also to restrict the number of unknown model parameters in the modeling. More accurate modeling of clustered air guns might provide better inversion results (as suggested by Laws et al. (1998)).

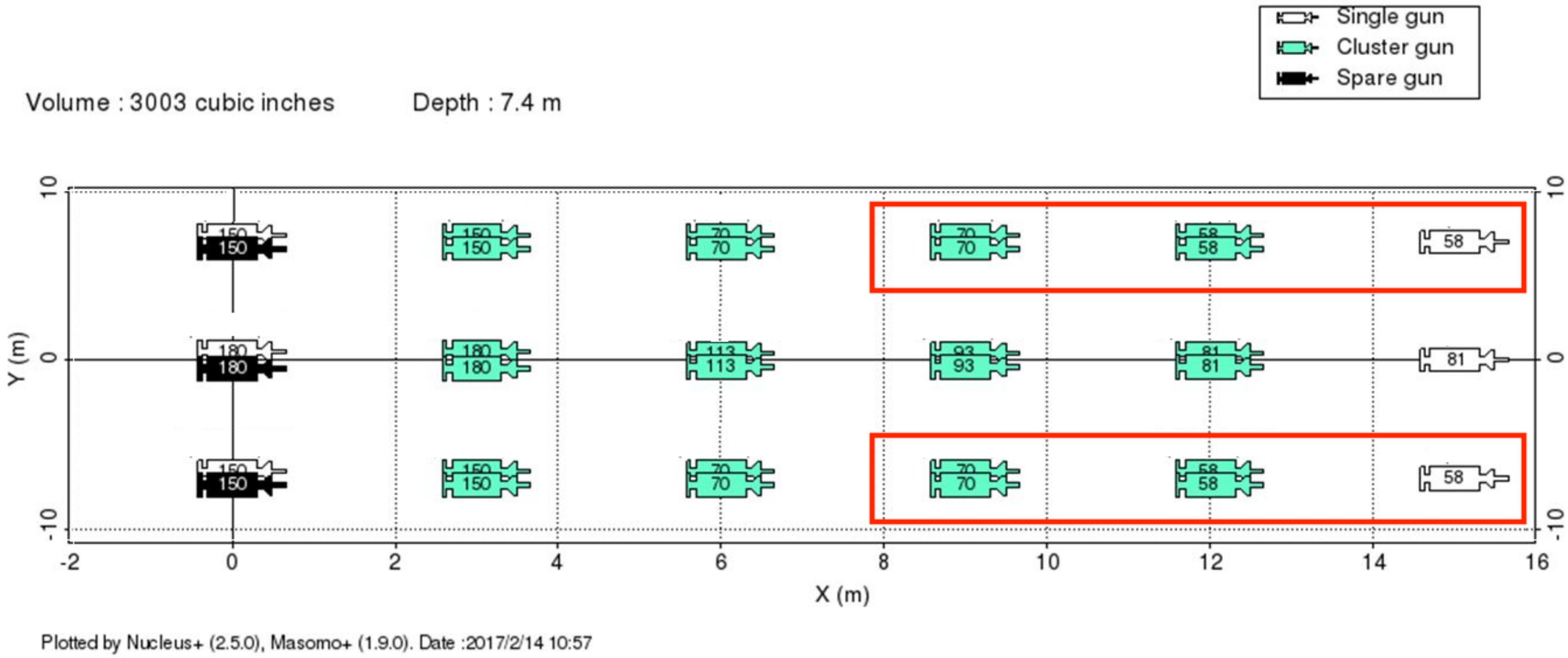

Figure 4.1: Source configuration (BroadSource) for the TopSeis tests in Gabon and over Frigg-Gamma. In total, there are 30 active air guns, at 6 and 9 m depth. The air guns in the red squares are placed at 9 m, whereas the other air guns are placed at 6 m. The figure is from the Nucleus software.

4.1.2 Instrument Filter

The instrument filter (the impulse response of the recording system) was a Seal LinP3 OUT 3-6 200-370 for both surveys. The impulse response of the filter (left) and the corresponding frequency spectrum (right) are shown in Figure 4.2. The instrument filter is included in the forward modeling of the synthetic data.

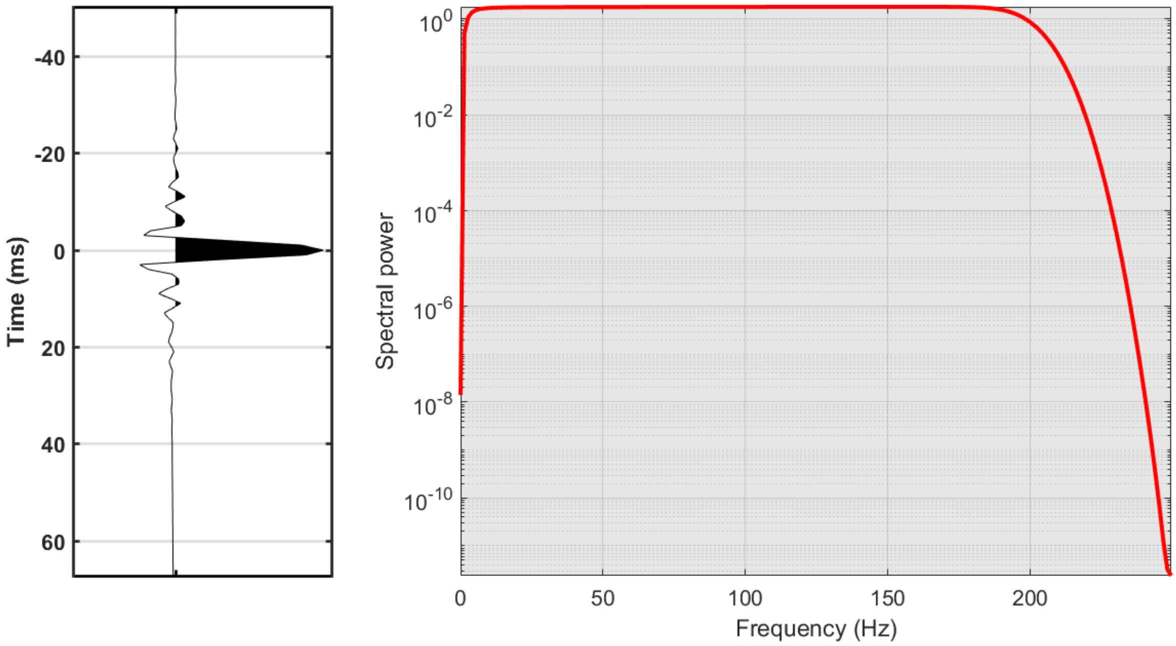

Figure 4.2: Impulse response (left) and frequency spectrum (right) of the instrument filter used in data acquisition.

4.2 Overloading of Receiver System

The hydrophones recording seismic data have a dynamic range, which is the ratio between the largest and smallest number that can be measured by the recording instrument. For conventional towed-streamer seismic, the dynamic range is usually sufficient to record the maximum amplitude of the direct wave. In TopSeis data, using industry standard Sentinel streamers, the amplitude of the direct wave measured directly below the source exceeds the dynamic range of the receiver system. Therefore, the receiver system is overloaded, and the direct wave is clipped as a consequence. To identify clipped traces, we compare the measured and modeled primary peak amplitude for shot 50 in the Gabon field test for receivers along the streamer closest to the source. The comparison is shown in Figure 4.3 and clearly demonstrates that the measured data is clipped between receiver number 6 and 12. Laws et al. (1998) experienced the same problem when they tested methods for source signature estimation, although they used smaller sources.

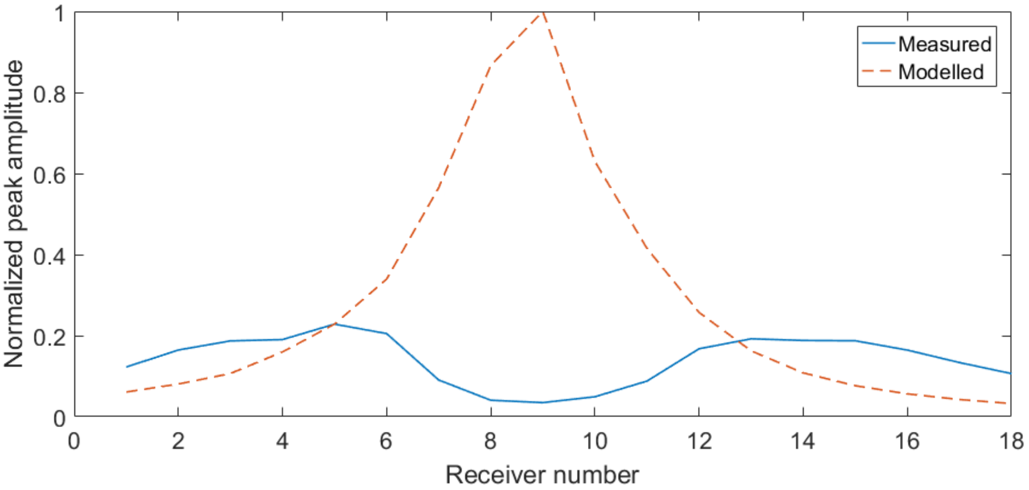

Figure 4.3: Measured (solid blue line) and modeled (dashed red line) primary peak amplitudes of streamer data for shot 50 in Gabon test. The measured primary peak is clearly clipped between receiver number 6 and 12.

We observe that the peak amplitude is not stabilizing at a maximum value corresponding to the upper limit of the dynamic range for the overloaded receivers, as one may expect. We compare three traces from the same shot with different offset and angle relative to the source in Figure 4.4 to illustrated how the measurements are damaged if they are clipped. The direct wave measured in the receiver closest to the source (blue) is clearly clipped, while the direct wave measured in the two other receivers are borderline clipped (red) and not clipped (yellow). It is evident from the figure why the measured peak amplitude is not stabilizing around a maximum amplitude for the overloaded receivers; the peak amplitude for the trace recorded closest to the source is not only clipped, it is also shifted in the direction of negative amplitude.

CGG has modeled the primary peak amplitude of the direct wave in the in-line direction, as shown in Figure 4.5. Clipping is expected to occur within the purple area, where the primary peak amplitude exceeds the dynamic range of the receiver system. For a streamer depth of ~35 m, receivers within offset of approximately 60 meters are expected to be overloaded. Due to source directivity, the clipping area is also asymmetric.

Also note in Figure 4.4 the late effect of the overloading of the receiver system in the measurements for the receiver closest to the source (blue). The receiver system is not recording accurately for some time after the primary peak has been recorded by the receiver. What appears

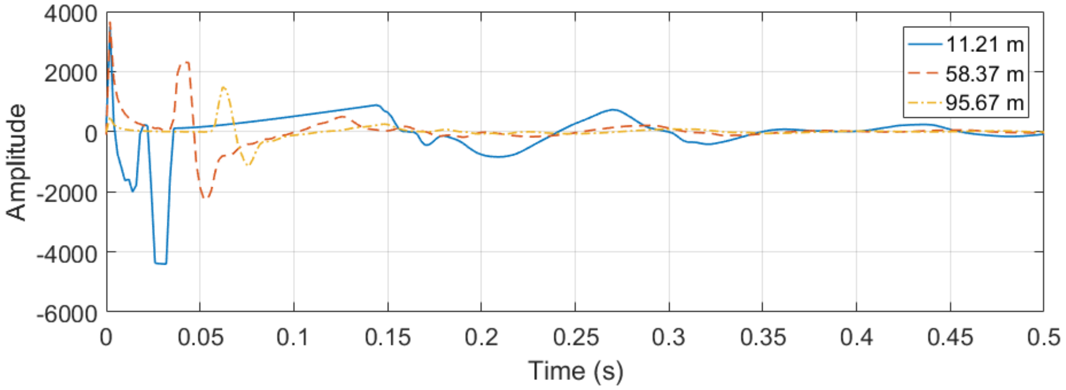

Figure 4.4: Plot with three different traces from shot 50 in Gabon test. The trace recorded at the receiver closest to the source (solid blue) is clearly clipped, while the two other are borderline clipped (dashed red) and not clipped (dashdotted yellow). The legend shows the offset between the source and each receiver.

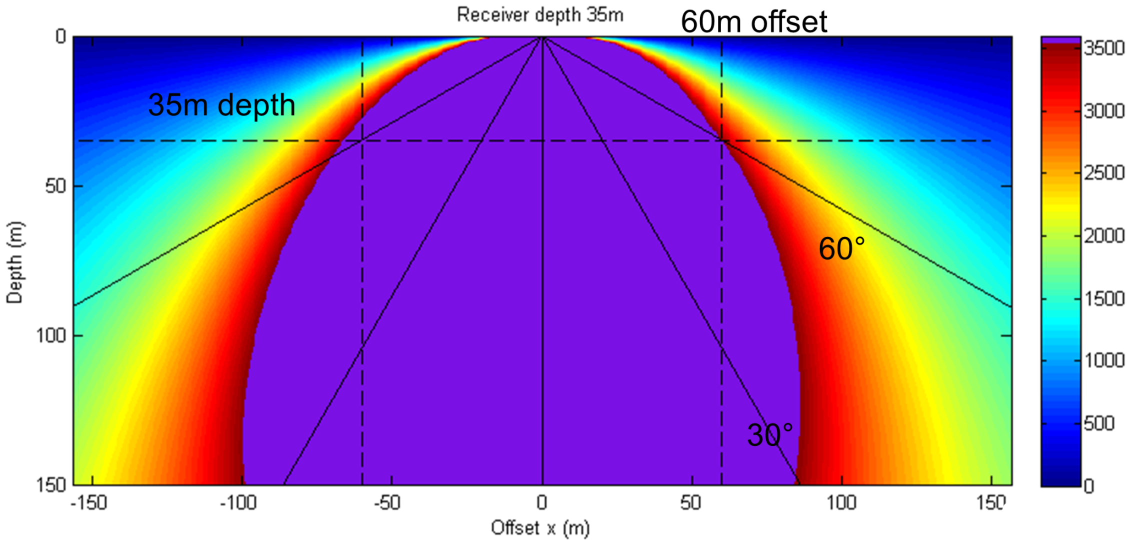

Figure 4.5: Plot of the primary peak amplitude of the direct wave in in-line direction. Clipping is expected to occur within the purple area, where the primary peak amplitude of the direct wave exceeds the dynamic range of the receiver system. For a streamer depth of 35 m, clipping will occur for offsets up to about 60 m. Figure courtesy of Carl-Inge Nilsen, CGG.

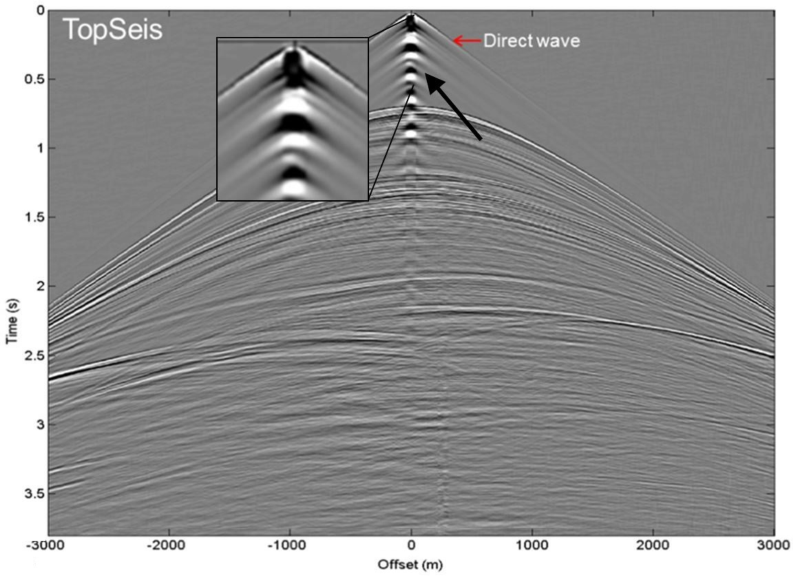

Figure 4.6: Shot-gather from TopSeis test in Gabon, with zoom on the clipped traces. The strong ringing at near-offset, highlighted by the black arrow, is most likely a late effect from the overloading of the receiver system. Figure courtesy of CGG.

to be the bubble in this trace is significantly stronger for the clipped trace, which is also evident in the near-offset traces in Figure 4.6, as highlighted by the black arrow. Additionally, there is an abrupt change in the amplitude of the bubble between the clipped and non-clipped traces in Figure 4.6. We have tested the inversion with the clipped traces included in the inversion (where the first 200 ms of the clipped traces have been muted out), and the estimated vertical far-field signature from the obtained notional source signatures has an unrealistically strong bubble compared to vertical far-field signatures from Nucleus and NFH-notionals. Hence, the strong ringing at near offsets is most likely a late effect of overloading of the receiver system, and not the bubble of the direct wave. Therefore, we do not include clipped traces in the inversion. It is not clear whether Laws et al. (1998) experienced similar ringing in the clipped traces of their data.

4.3 Deepwater Data: Offshore Gabon

In March 2016, CGG Marine acquired a 2D test line offshore Gabon, where the acquisition parameters are provided in Table 4.1.

Acquisition parameter	**Value**
Temporal sampling rate [ms]	2
Record length [ms]	5000
Number of streamers	10
Streamer separation [m]	100
Streamer length [km]	10
Receiver spacing [m]	12.5
Number of sources	2
Source separation [m]	50
Source volume [cu.in.]	3003
Shot point interval, flip-to-flip [m]	37.5
Water depth [m]	~720

Table 4.1: Acquisition parameters for 2D test offshore Gabon.

In Figure 4.7 we display a shot-gather with the receivers along the streamer closest to the source for the shot used in the inversion. The bubble of the direct wave is uncontaminated by reflections, due to the water depth of ~720 m.

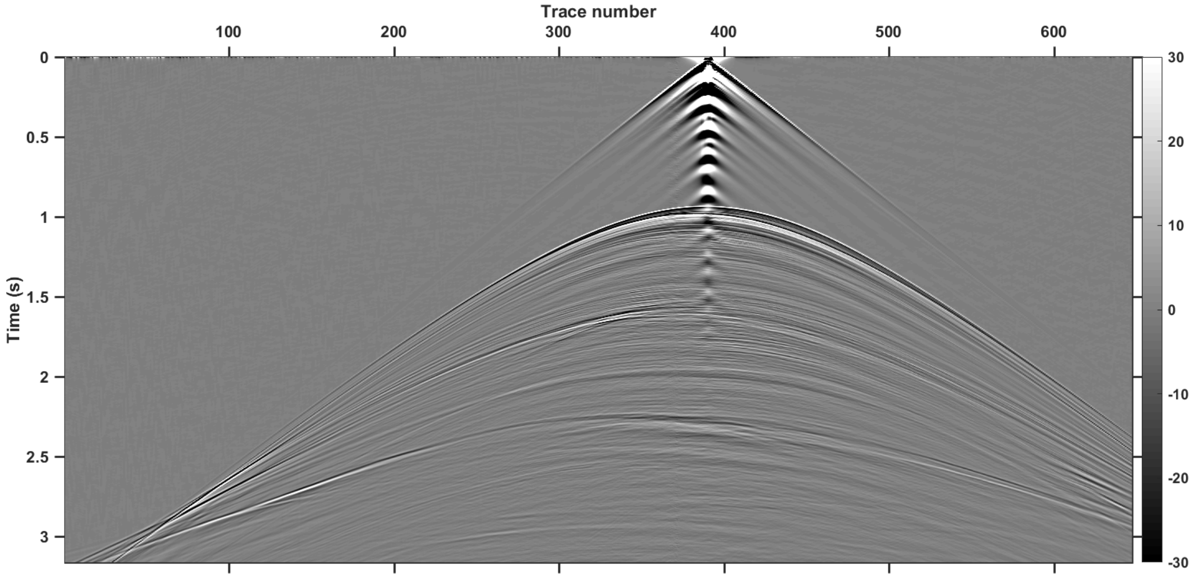

Figure 4.7: Shot-gather from streamer closest to source for shot 50 in Gabon test. Note that we have a clean recording of the direct wave up to about 1 second, even for relatively long offsets, due to the deep water.

4.3.1 Data Preparation

Due to the late effect of the overloading of the receivers at near offsets, these traces cannot be used in the inversion algorithm. As mentioned in Section 4.2, CGG has found that as a rule of thumb, receivers within offset of 60 m have been overloaded. We use receivers with a minimum offset of 70 meters in the inversion, where we have a margin of error because the clipping area might vary with acquisition geometry and in inline/crossline direction. The maximum offset is set to 125 meters. Offsets between 70 and 125 m correspond to departing angles for the direct wave of ~66-76° relative to the vertical. Figure 4.8 shows the receivers with offset between 70 to 125 meters and the position of all the air guns in the source array. As can be seen from the figure, receivers from three of the streamers are used in the inversion. The receivers are numbered as indicated in the figure for later in this section.

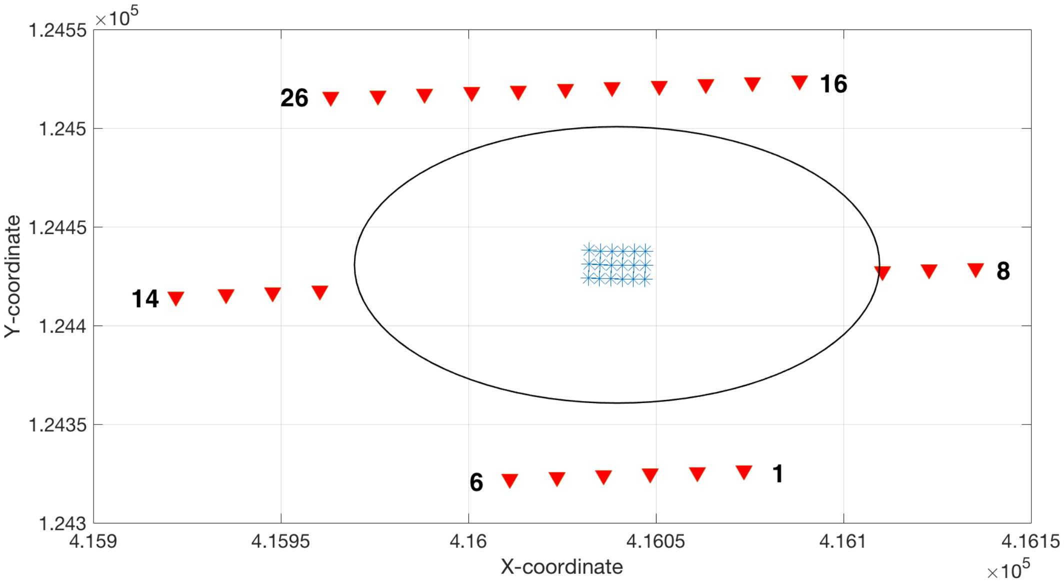

Figure 4.8: Coordinates for air guns (blue crosses) and receivers used in inversion (red triangles) from the Gabon test. The black circle shows the approximate boundary between overloaded and not overloaded receivers. The receivers are numbered as indicated for later plots in this section. Note that only 18 air guns are plotted here, because we assume that a cluster of two air guns can be described as one single air gun.

Prior to running the inversion algorithm, we also corrected for a rotation of the source array relative to the streamers. The source rotation is due to that the sail line direction of the source vessel was slightly different from the sail line direction of the streamer vessel, but this was not corrected for in the provided source position in the header of the seismic data. If we consider two consecutive shots, the sail line direction of the source and streamer vessel can be calculated,

$$\phi_s = \tan^{-1}\left(\frac{y_{s2} - y_{s1}}{x_{s2} - x_{s1}}\right) \tag{4.1}$$

$$\phi_r = \tan^{-1}\left(\frac{y_{r2} - y_{r1}}{x_{r2} - x_{r1}}\right) \tag{4.2}$$

where ϕ_s and ϕ_r are the sail line direction of the source and streamer vessel, x_{s1}, y_{s1}, x_{s2} and y_{s2} are the source center coordinates for each shot and x_{r1}, y_{r1}, x_{r2} and y_{r2} are the receiver coordinates for a given receiver for each shot. The rotation of the source relative to the streamer vessel's sail line is $\phi_{diff} = \phi_r - \phi_s$, and the source can then be rotated accordingly.

4.3.2 Inversion Results

The inversion was carried out for one shot in the Gabon data set with the receivers shown in Figure 4.8. Some of the details about the inversion are provided in Table 4.2.

Parameter	**Value**
Initial error [%]	47.2
Final error [%]	34.2
Iterations for first frequency window	7
Total number of iterations	13

Table 4.2: General information about inversion for deepwater data set.

The water depth of ~720 m means that we have a clean recording of the direct wave in the traces that were used in the inversion. This can be seen in Figure 4.9, where the real data in a shot-gather are shown at the top. Also shown in Figure 4.9 are the estimated data in a shot-gather after the inversion (middle) and the residuals (bottom). The gathers are divided into three boxes, corresponding to the three streamers that were included in the inversion. The traces are gained (multiplied by t) to make the bubble more visible. The errors in the primary peak and source ghost appears to contribute to most of the error between the real and modeled data, whereas the bubble seems to be well estimated up to about 300 ms, especially for the bubble time period. The large dissimilarities in primary peak and source ghost are most likely due to the complexity of the wavelet of the dual-level three-string source configuration in the crossline-direction, as evident from the real data in Figure 4.9. Therefore, the inversion will be very sensitive to errors in the source and receiver positions in these directions. This is also apparent from Figure 4.10, where the initial and final error - trace by trace - is shown. The error is largest in the receivers at high departing angles in the outer streamers.

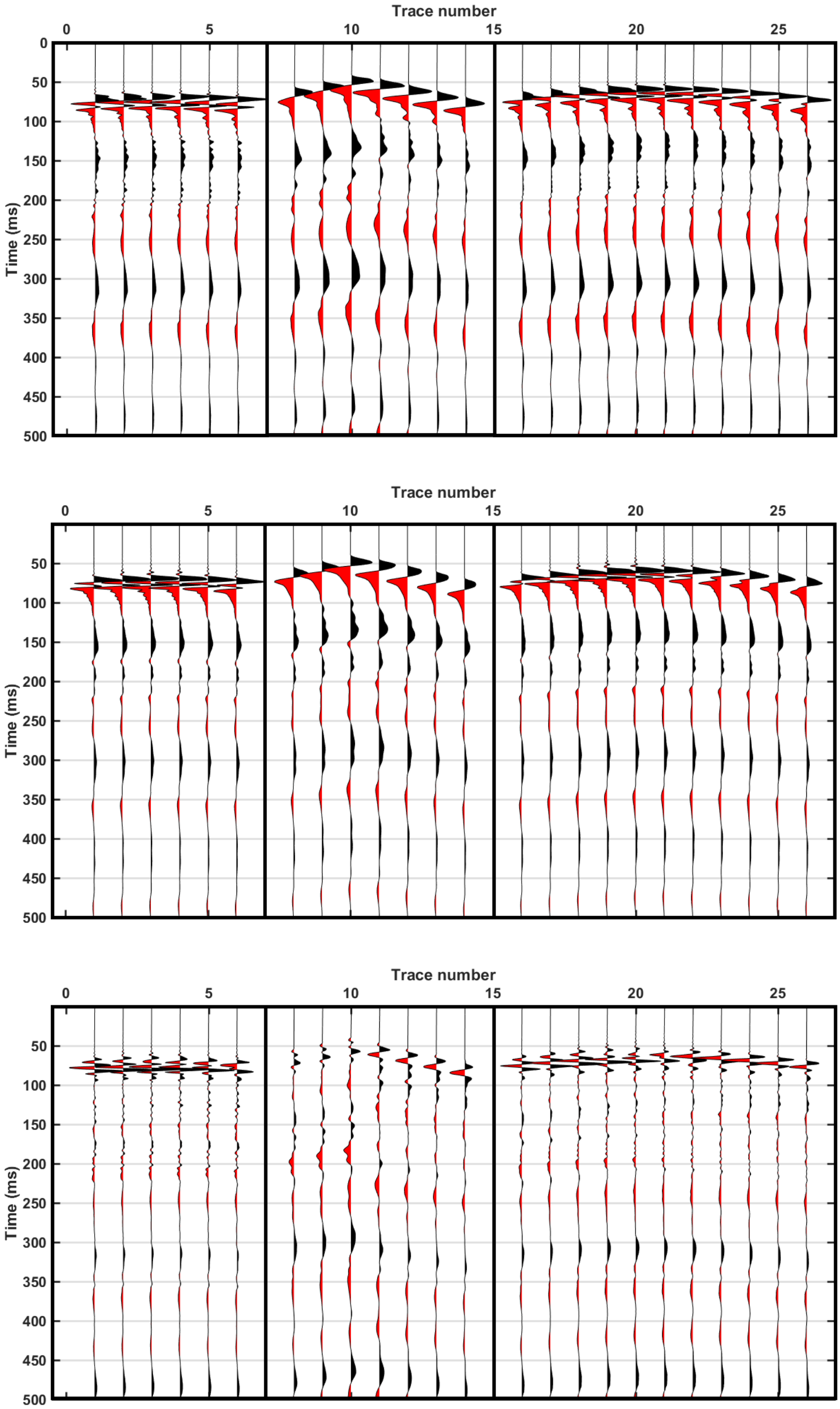

Figure 4.9: Top: Real data. Middle: Modeled direct wave after inversion. Bottom: Difference. A t-gain is applied to the data to make the bubble more visible. The relative error between the real data and the modeled direct wave from the initial model was 47.2%, while the error was 34.2% after the inversion. Each box correspond to receivers from one streamer. Notice that there are large differences between the real and modeled peak/source ghost at the outer streamers.

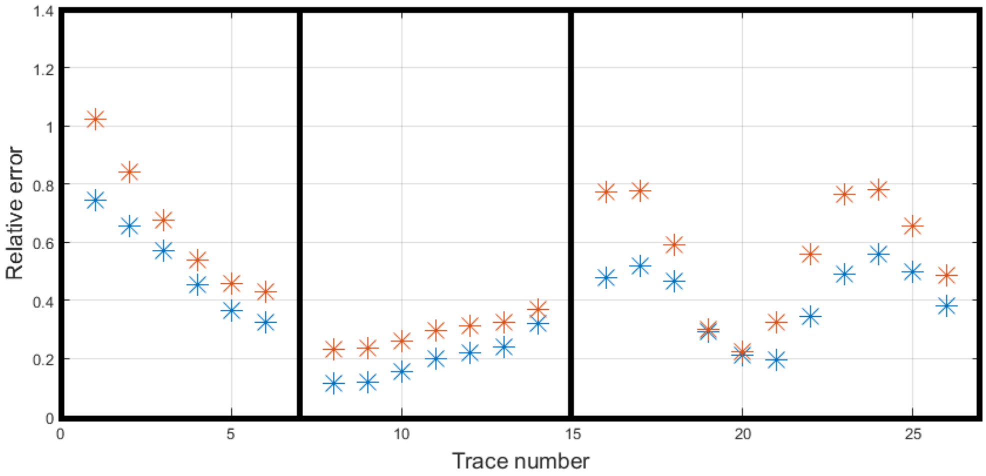

Figure 4.10: Initial (red) and final (blue) error, trace by trace. Most of the minimization occurs at receivers at high departing angles, due to the complexity of the wavelet from the dual-level source at these angles. Each box correspond to receivers from one streamer.

In Figure 4.11, we show the initial (red) and estimated (blue) model parameters for each air gun; α (top left), β_0 (top right), β_1 (bottom left) and firing time delay (bottom right). The sea surface reflection coefficient was estimated to -0.9504, while the initial value was -1. We also show the initial (red) and final (blue) streamer depths in Figure 4.12. The largest discrepancies are observed in the outer streamers, which again highlights the sensitivity of the inversion with regards to errors in the receiver positions in the outer streamers.

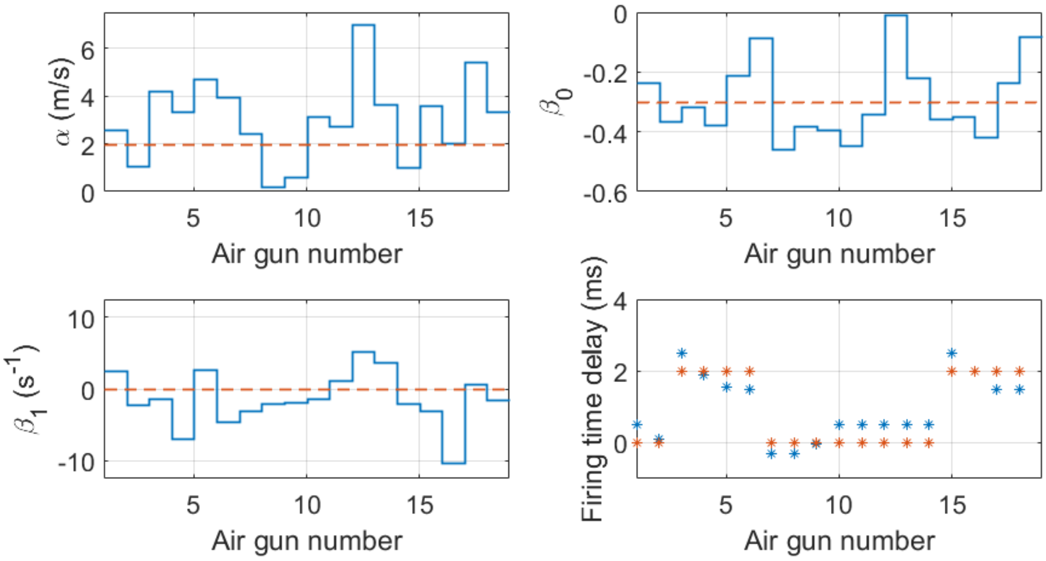

Figure 4.11: Initial (dashed red) and estimated (solid blue) model parameters after inversion. Top left: α, top right: β_0, bottom left: β_1 and bottom right: firing time delay.

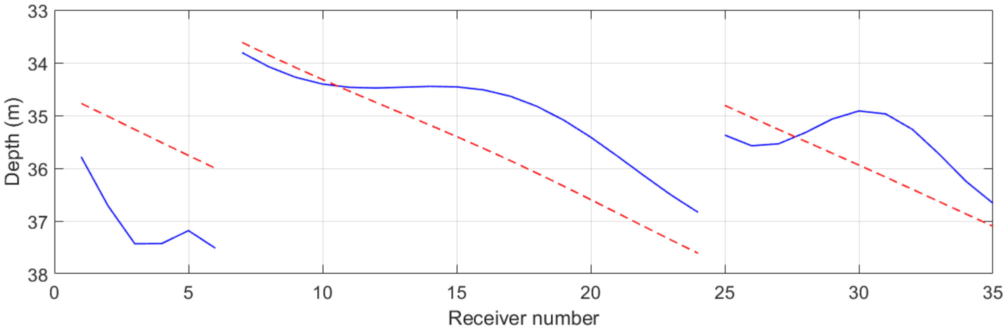

Figure 4.12: Initial (dashed red) and estimated (solid blue) streamer depth for each streamer. Receiver number 10-19 were not included in inversion due to clipping. Note that the receivers are here numbered differently than in the other figures in this section.

From the estimated α, β_0 and β_1-values, we can calculate the notional source signatures for each air gun in the air gun array, based on the physical modeling of a bubble, explained in Section 3.2. In Figure 4.13, we show the estimated notional source signatures from NFH-measurements (top) and from the inversion (bottom). The notional source signatures from the two methods are different, but they also describe the same physics, especially with regards to the bubble time period. The notional source signatures from NFH-measurements have residual source ghosts, e.g. where highlighted by the blue arrow. This is because the notional source signatures are estimated from actual measurements in the near-field, where non-linear dynamics make it challenging to remove the contribution from neighbouring air guns and ghosts from the measurements in each near-field hydrophone. Contrary, the notional source signatures from the inversion will not include residual source ghosts, because they are based on physical modeling of the bubbles from the air guns. Also note that there are dissimilarities in the amplitude of the primary peak for some of the estimated notional source signatures. An example of this is notional number 6, where the grey circles highlight the large differences in estimated primary peak amplitude from the two methods.

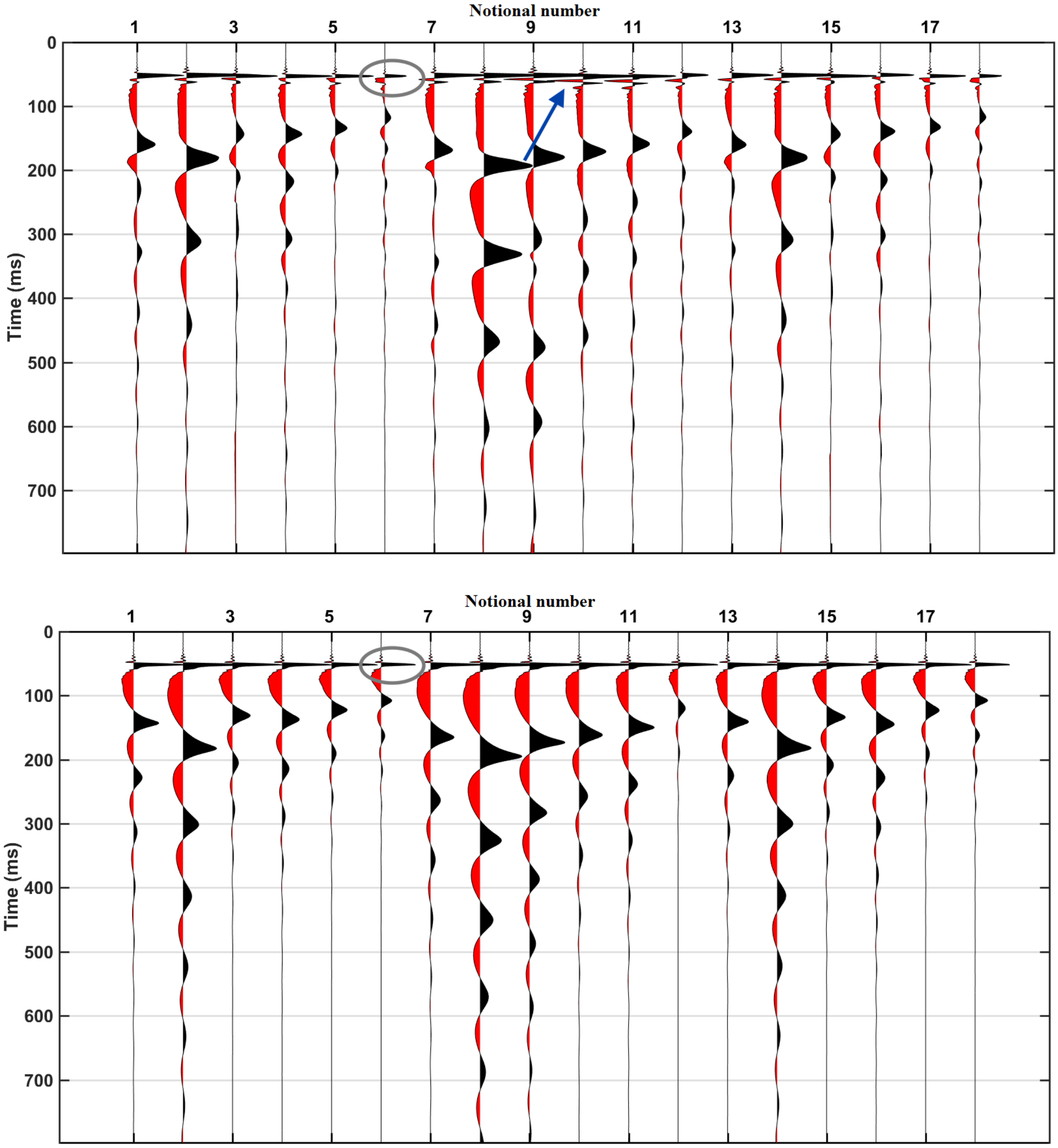

Figure 4.13: Top: Notional source signatures from near-field hydrophone measurements. Bottom: Notional source signatures estimated from the direct wave. Note that there are residual ghosts in the notional source signatures from near-field hydrophones (highlighted by the blue arrow). There are also large differences in the amplitude of the primary peak for the two methods, see e.g. the amplitude difference for notional 6 (see the grey circles).

Based on the notional source signatures from the inversion and from near-field hydrophone measurements, we can estimate the direct wave recorded at the streamers and compare it with the recorded direct wave. Here, we extrapolate the notionals to the initial receiver positions, not the estimated receiver positions from the inversion, as was done for the modeled data from the inversion (Figure 4.9). In Figure 4.14, we show: Top left: Real data for trace number 11 (left), modeled direct wave from inversion (middle) and modeled direct wave from NFH-notionals (right). Top right: Real data for trace number 11 (left), difference between real and estimated direct wave from inversion (middle) and difference between real and estimated direct wave from NFH-notionals (right). At the bottom, we show the similar, but for trace number 20. The traces are gained (multiplied by t) to make the bubble more visible. The bubble of the direct wave appears to be better estimated with the notional source signatures from the inversion up to about 200-250 ms for both traces, while it is better estimated from the NFH-notionals after 250 ms. The estimated bubble from the inversion has the wrong polarity from around 400 ms for both traces.

To illustrate the error in the estimated bubble for all the traces, we compare the cumulative error between the real data and the estimated direct wave from the two sets of notional source signatures in Figure 4.15, where we disregard the first 100 ms because we are interested in the differences in the estimated bubble. It is evident from the figure that the notional source signatures from the inversion estimate the bubble of the direct wave more accurately up to about 250 ms, as the black arrow at 200 ms highlight. Also evident from the figure, is that the later part of the bubble is better estimated with the NFH-notionals. The increase in cumulative error around 0.45 s for the notionals from the inversion, highlighted by the second black arrow, correspond to where the estimated direct wave has the wrong phase and amplitude for the traces in Figure 4.14.

The notional source signatures from the inversion and from the NFH-measurements can also be used to estimate vertical far-field signatures below the source. We compare the estimated vertical far-field signatures with a vertical far-field signature from Nucleus in Figure 4.16, in time- (top) and frequency-domain (bottom). The sea surface reflection coefficient is set to -1 in all cases, and firing time delays are the same. The primary peak and source ghost in the far-field signature from the inversion matches the Nucleus-signature well, whereas the primary peak and source ghost estimated from near-field hydrophones are very different. This is especially evident

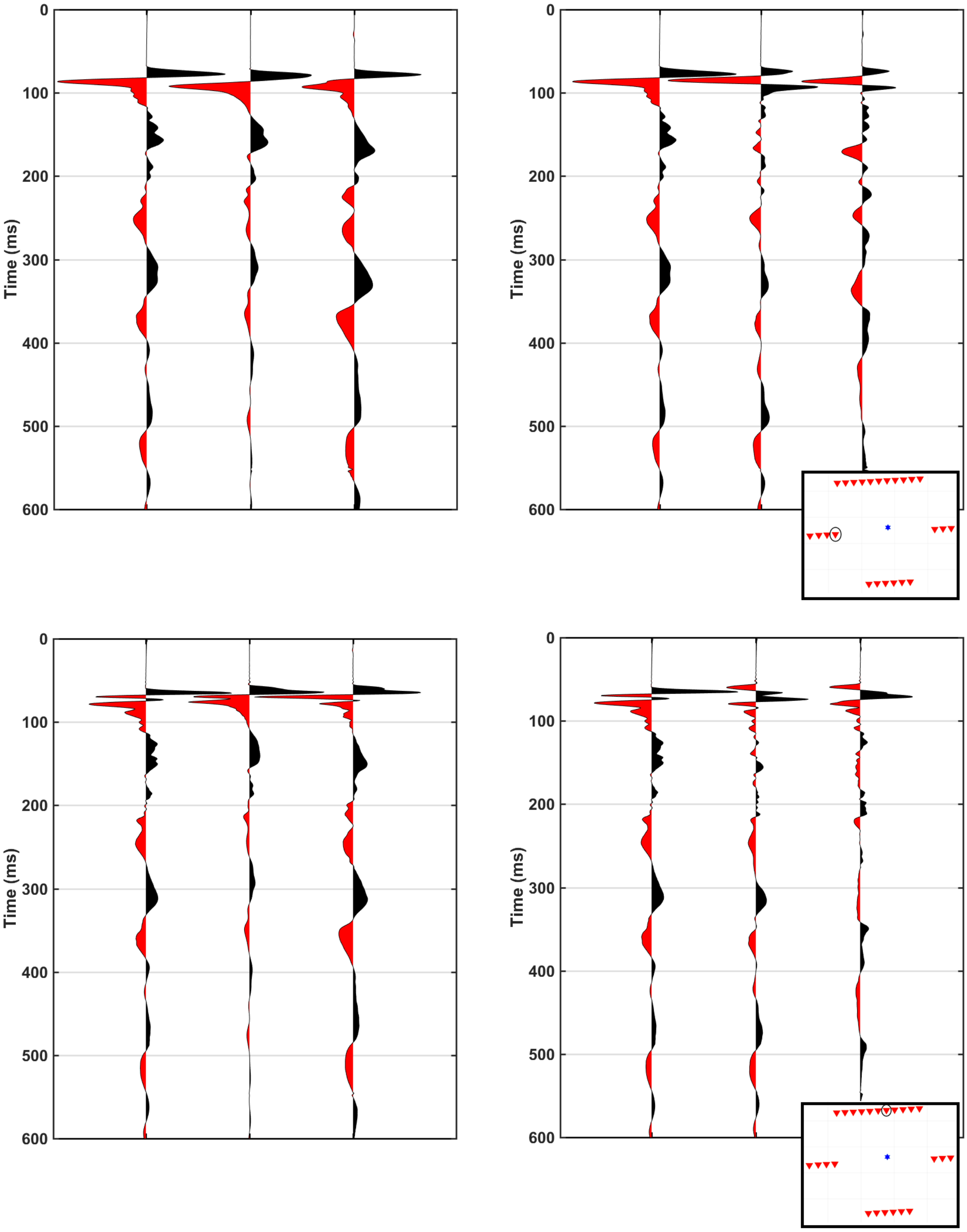

Figure 4.14: Top left: Real data, trace 11 (left), estimated direct wave for trace 11 from inversion (middle) and estimated direct wave for trace 11 from notional source signatures from NFH-measurements (right). Top right: Real data, trace 11 (left), difference between real data and estimated direct wave from inversion (middle) and difference between real data and estimated direct wave from notional source signatures from NFH-measurements (right). Bottom: Similar, but for trace 20. The receiver positions relative to the source are circled in in the two maps. For both traces, the bubble appear to be better estimated up to ~300 ms with the notional source signatures from the inversion. The traces are plotted with a t-gain to make the bubble more visible.

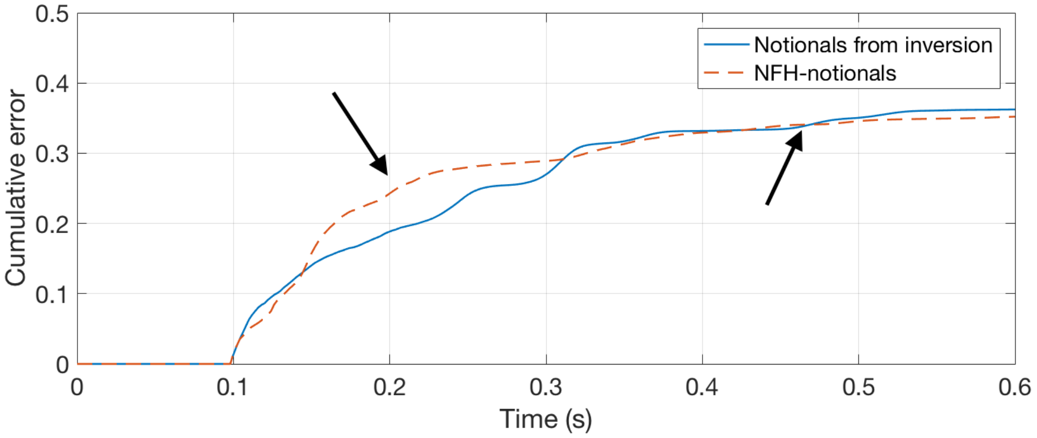

Figure 4.15: Cumulative error (for all traces) for estimated direct wave from inversion (blue) and notional source signatures from NFH-measurements (dashed red). The notional source signatures from the inversion estimate the bubble better between 0.1 and 0.25 s. We disregard the relative error for the first 0.1 s because we want to observe the differences in estimated bubble, not primary peak/source ghost here. The arrow at 0.2 s shows the large differences in accuracy for the estimated bubble from NFH-notionals and from inversion up to 0.25 s, whereas the black arrow at 0.45 s show the increase in cumulative error for the notionals from inversion due to estimation of wrong polarity of the direct wave.

in the frequency spectrum, where the notches from the source ghost occur in different frequency regions for the far-field estimated from NFH-notionals. The residual ghost in the NFH-notionals will create a tuning effect when the source ghost is added to the far-field signature, and this is most likely what is observed here.

With regards to the bubble, there are large differences between the three estimated vertical far-field signatures, highlighted by the zoom in the time- and frequency plots. Note that the modeling of the direct wave with the notional source signatures from the inversion was more accurate than the NFH-approach up to about 150 ms after the direct wave, as evident from the cumulative error in Figure 4.15. Hence, the estimated bubble from the inversion should be relatively accurate within this time window, given that the notional source signatures from the inversion can be used to extrapolate vertical far-field signatures accurately.

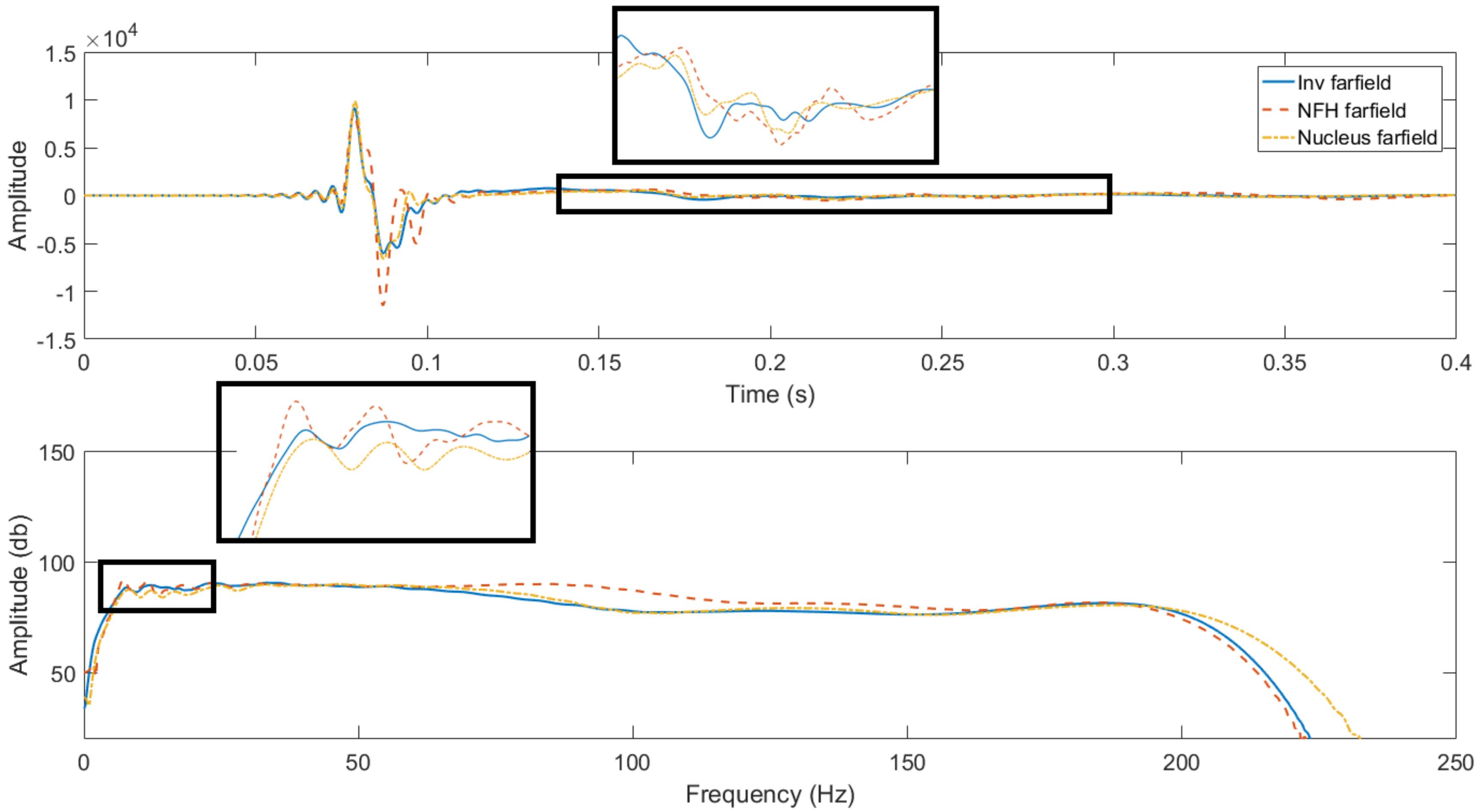

Figure 4.16: Top: Estimated vertical far-field signatures 5000 m below source array from notional source signatures by inversion (solid blue), NFH-notionals (dashed red) and Nucleus signature (dashdotted yellow). Bottom: Corresponding frequency spectrum. The primary peak and source ghost from the inversion corresponds well with the far-field signature extracted from Nucleus, while the estimated peak and source ghost are inaccurate for the NFH-method, due to the residual ghost present in the notional source signatures. The zoom in the plots reveal the large differences in estimated bubble from the three methods. NB: Note that the scale of the zoom is different from the scale of the full figure.

4.3.3 Source Designature Results

The estimated notional source signatures from the inversion and from NFH-measurements can be used as input in a standard designature flow (where the theory is explained in Section 3.4). The designature flow is specially designated for the water bottom reflection, as the departing angle can be directly calculated if the source and receiver positions and water depth is known, assuming that the water bottom is flat (i.e. the income angle is equal to the reflection angle relative to vertical) and that the velocity in the water layer is constant (i.e. there is no ray bending in the water layer). We have here used the estimated sea surface reflection coefficient of -0.9504 when the source ghost is added to the far-field signature. The desired output wavelet is shown in Figure 4.17, in time- (left) and frequency-domain (right). The corner frequencies in the spectrum are 4,7, 80 and 120 Hz.

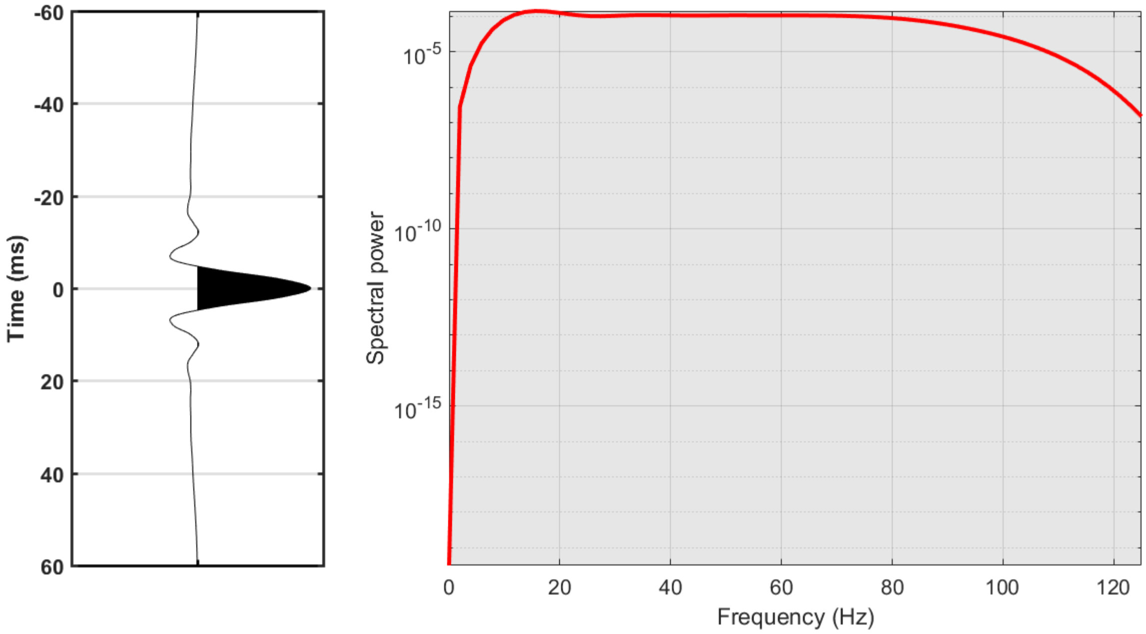

Figure 4.17: Desired wavelet for designature in time (left) and frequency domain (right). The corner frequencies of the spectrum are 4, 7, 80 and 120 Hz.

The designature was applied to 150 traces along the streamer closest to the source, as shown in Figure 4.18. The traces where clipping was most severe, colored black in Figure 4.18, were muted before the designature because the ringing after the direct wave affected the stability of the designature algorithm.

Figure 4.19 shows common shot-gathers before designature (left) and the data after designature with the notional source signatures from the inversion (middle) and from NFH-measurements

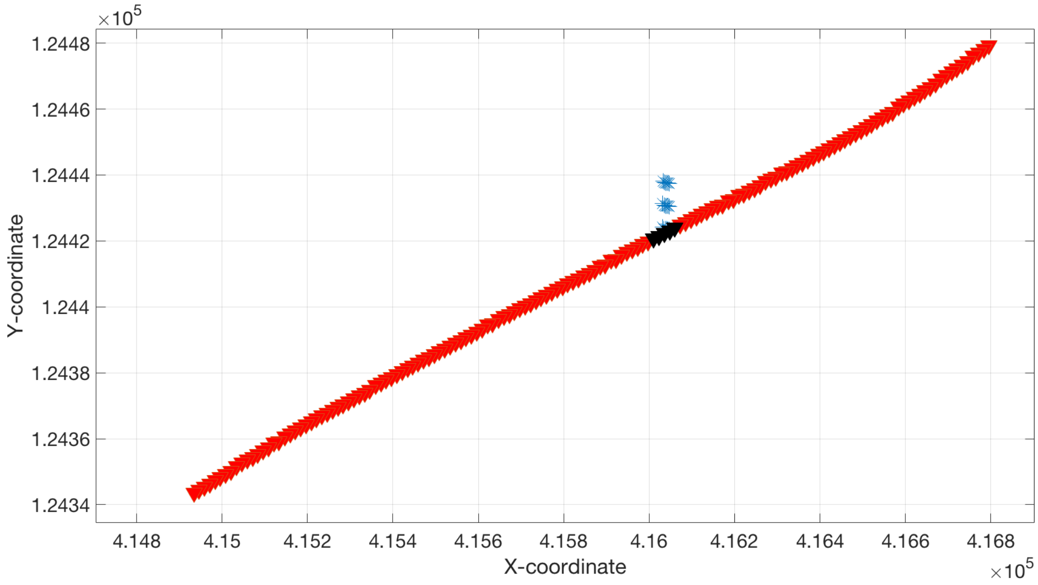

Figure 4.18: Map showing position of receivers (red triangles) included in designature flow relative to positions of air guns (blue crosses). The receivers colored black were muted prior to designature.

(right). The water bottom reflection is expected to be zero-phase after the designature, because the shallow geology is dipping, so there is little tuning and interference with other reflections. The designature with both sets of notional source signatures appear to zero-phase the water bottom reflection and the associated receiver ghost, but the zero-phasing seems to be more successful with the notional source signatures from the inversion.

The debubbling, i.e. the zero-phasing of the bubble, is more difficult to assess. Residual bubble energy from the water bottom reflection will appear as low-frequency signal in the gathers with the same move-out as the water bottom reflection. To compare the residual bubble energy in the two gathers after designature, we align the data so the water bottom reflection is horizontal. Because residual bubble energy will have the same move-out as the water bottom reflection, it will also appear as horizontal events after the alignment. The gathers after the alignment are shown in Figure 4.20, input data (left), after designature with notional source signatures from the inversion (middle) and from NFH-measurements (right). The black arrow in the gather to the right highlights a low-frequency event with horizontal move-out that is not apparent in the gather from designature with the notional source signatures from the inversion. We can also observe that the receiver ghost does not appear as a horizontal event due to the variable-depth streamer profile CGG has used during acquisition.

While the reflection from the water bottom will appear horizontally after the alignment, other events will have upwards move-out, due to higher apparent velocity. Therefore, we can stack the traces in the aligned gathers to enhance the residual bubble from the water bottom reflection. In Figure 4.21, we show the stack of the traces designatured with notional source signatures from the inversion (left), notional source signatures from NFH-measurements (middle) and the difference (right). The water bottom reflection, highlighted by the black arrow in the trace to the left, is better zero-phased with the notional source signatures from the inversion. This is due to the better estimated primary peak and source ghost, as discussed previously. The receiver ghost appear as a smeared event in both traces, because it stacks out due to the variable-depth streamer profile.

With regards to the bubble, the designature with notional source signatures from NFH-measurements has residual low-frequency signal, especially evident where we have highlighted with circles. The residual low-frequency energy in the circle at 1000-1050 ms correspond to the low-frequency event highlighted by the black arrow in Figure 4.20. The low-frequency energy in the second circle also appear to be residual bubble energy, but this is more difficult to explain as the NFH-notionals modeled the direct wave at the streamers relatively accurate in this time window. The low-frequency energy is also apparent in the trace of the difference between the two. The time period appears to be ~90 ms, which is typical for the bubble time period for modern air gun arrays.

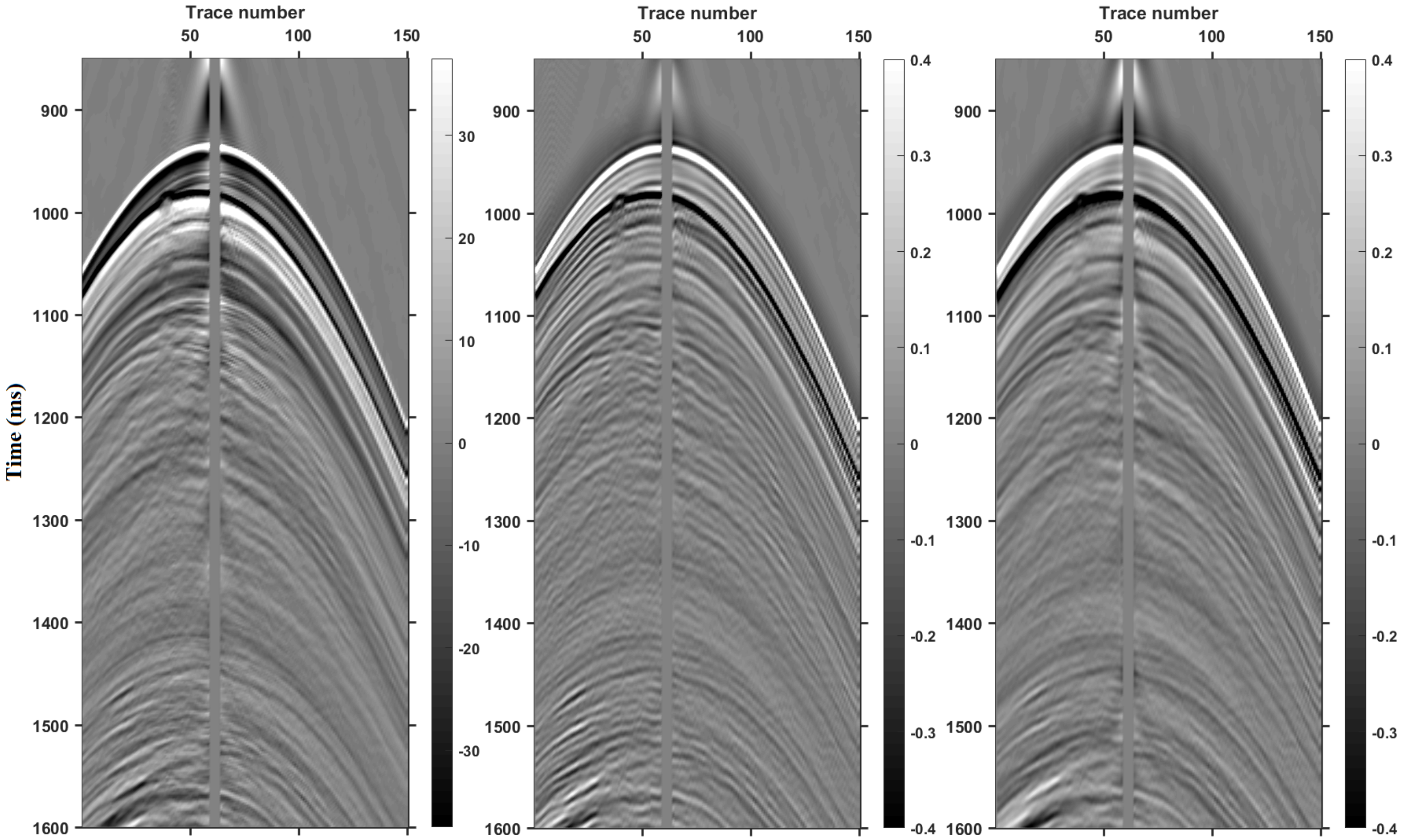

Figure 4.19: Results after designature. Left: Shot-gather prior to designature. Middle: After designature using notional source signatures from the inversion. Right: After designature with notional source signatures from NFH-measurements. Trace number 60-64 are muted before the designature, due to severe ringing in these traces.

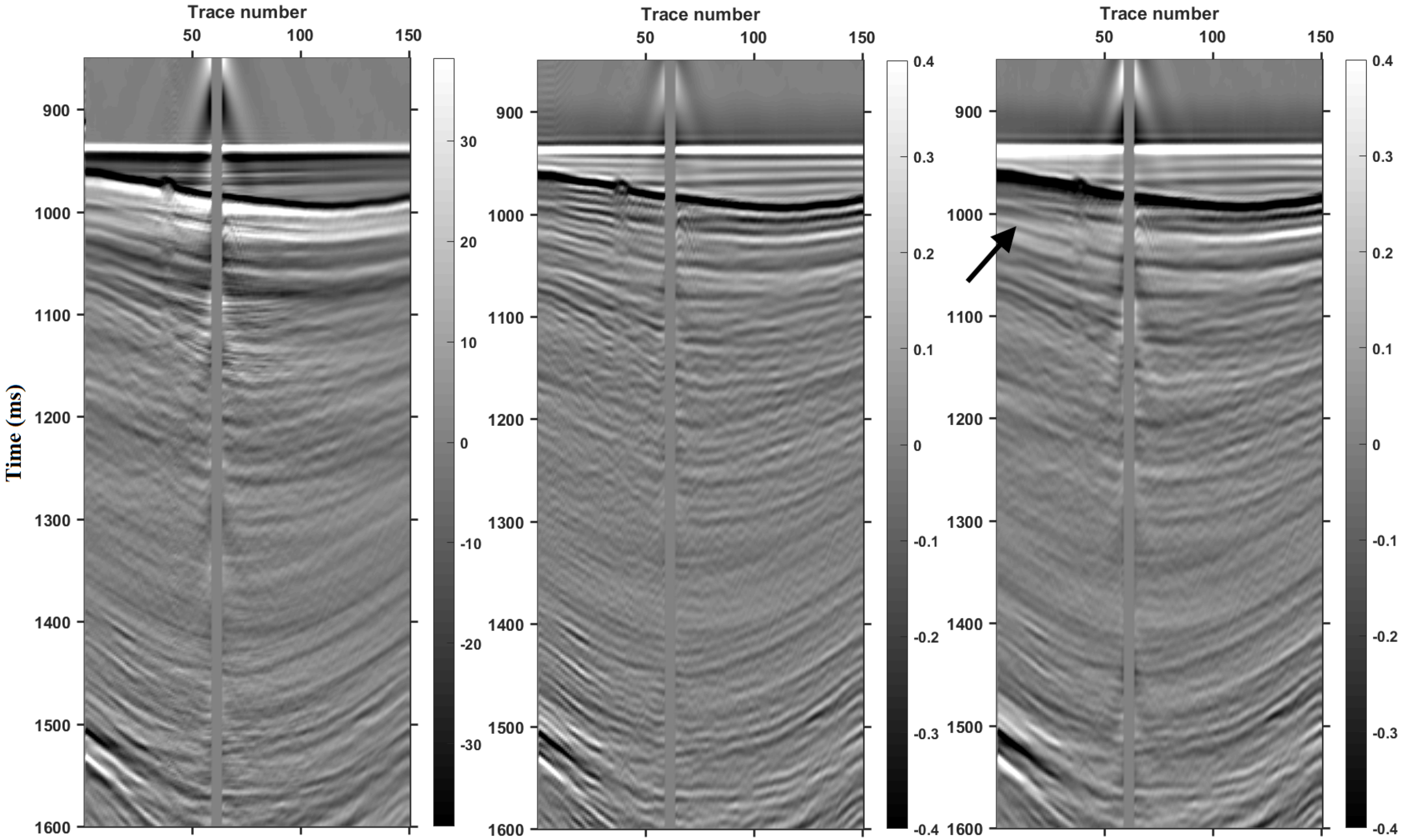

Figure 4.20: Results after aligning water bottom reflection. Left: Shot-gather prior to designature. Middle: After designature using notional source signatures from the inversion. Right: After designature with notional source signatures from NFH-measurements. Trace number 60-64 are muted before the designature, due to severe ringing in these traces. Deeper reflections have move-out upwards because aligning the WB reflection will over-correct the move-out of deeper reflections (with higher apparent velocity). The arrow in the gather to the right highlight a low-frequency event that can be residual bubble energy.

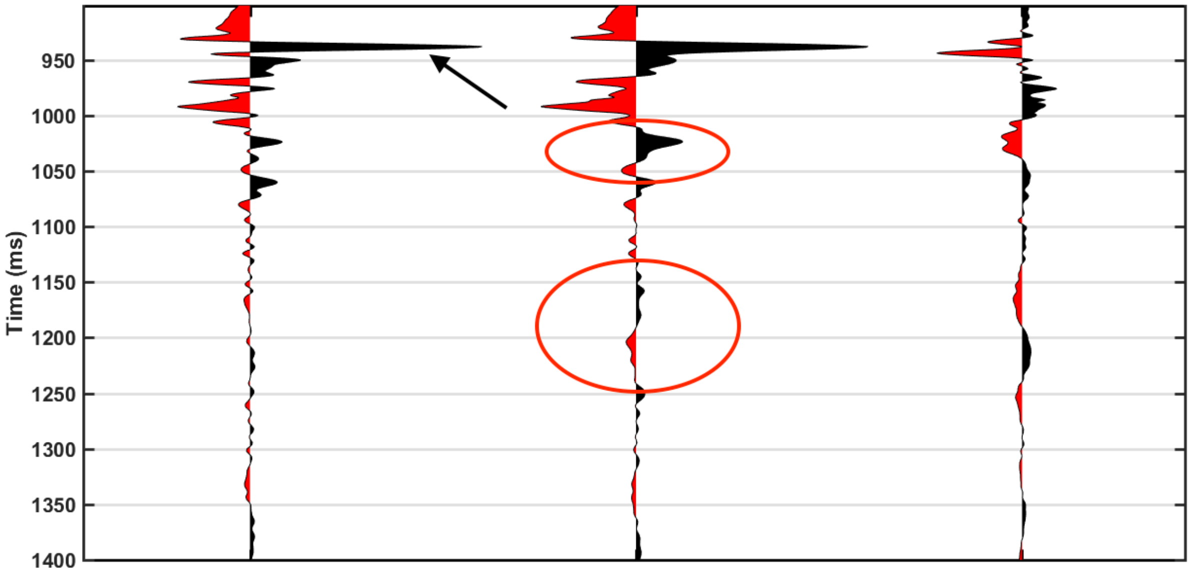

Figure 4.21: Left: Stack of the designatured traces with notional source signatures from inversion. Middle: Stack of the designatured traces with notional source signatures from NFH-measurements. Right: Difference. The designature with notional source signatures from NFH-measurements have more low-frequency energy, especially where highlighted with red circles. The water bottom reflection (highlighted by the black arrow) is better zero-phased with the notional source signatures from the inversion due to better estimation of the primary peak and source ghost in the far-field signature. The receiver ghost stacks out due to the variable-depth streamer profile used during acquisition.

4.4 Shallow Water Data: Frigg-Gamma Field

In June 2016, the first 3D test using TopSeis was conducted over the Frigg-Gamma structure in the central Northern North Sea using seismic vessels acquiring data for CGG's Multi-Client & New Ventures group. A small, rectangular full-fold area of 15x3 km extending south-to-north was selected, as the map in Figure 4.22 illustrates.

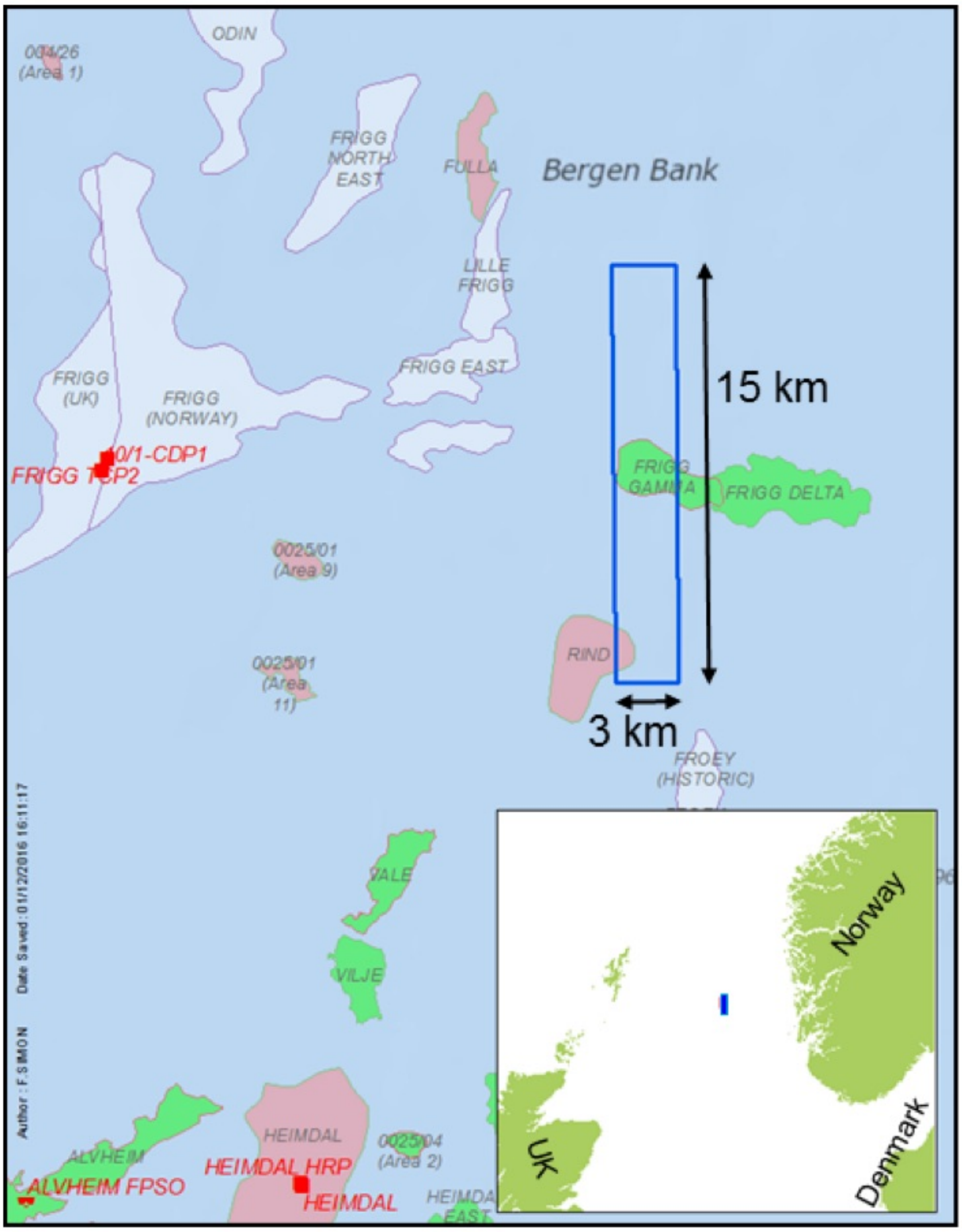

Figure 4.22: TopSeis 15x3 km 3D test area over Frigg-Gamma in the North Sea.

The acquisition parameters are provided in Table 4.3 and a shot-gather for the streamer closest to the source is shown in Figure 4.23. The bubble of the direct wave is now contaminated by reflections from the subsurface, due to the shallow water depth of ~120 m.

Acquisition parameter	**Value**
Temporal sampling rate [ms]	2
Record length [ms]	6000
Number of streamers	12
Streamer separation [m]	75
Streamer length [km]	8.8
Receiver spacing [m]	12.5
Number of sources	2
Source separation [m]	112.5
Source volume [cu.in.]	3003
Shot point interval, flip-to-flip [m]	25
Water depth [m]	~120

Table 4.3: Acquisition parameters for 3D test over Frigg-Gamma.

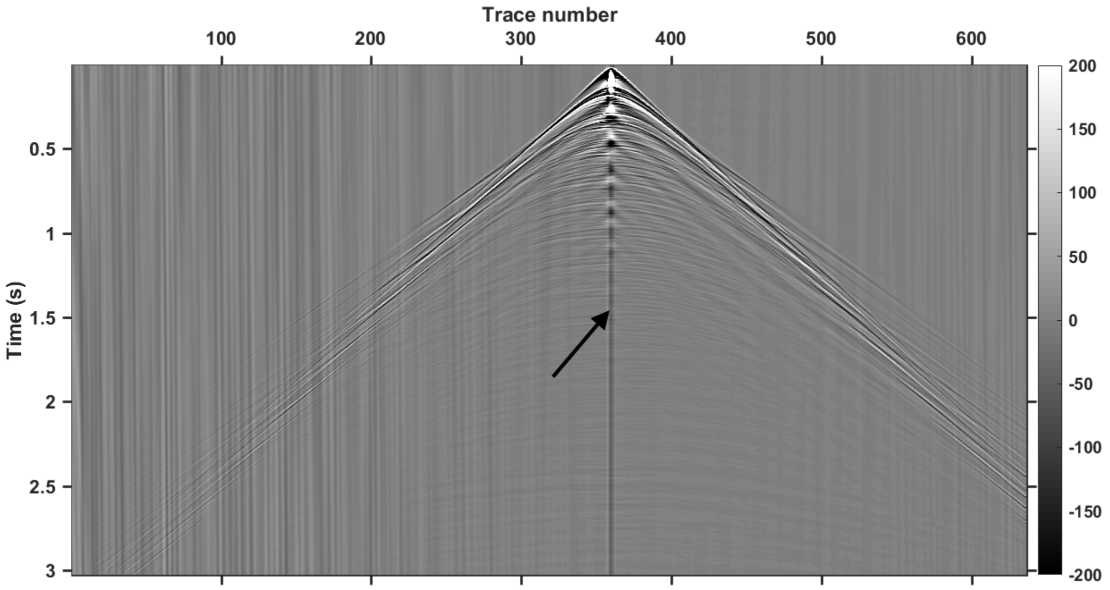

Figure 4.23: Shot-gather from streamer closest to source for shot 2544 in Frigg-Gamma test. The bubble of the direct wave is contaminated by reflections. A DC shift is observed at near-offsets, as highlighted by the black arrow.

4.4.1 Data Preparation

A DC shift was observed in the raw data from the acquisition over the Frigg-Gamma field (see near-offsets in Figure 4.23, highlighted by the black arrow.). The DC shift is energy at 0 Hz in the frequency-domain, and can therefore be removed with a low-cut filter with a steep slope. This is evident in Figure 4.24, where a trace is shown before and after a 2.5 Hz low-cut filter is applied.

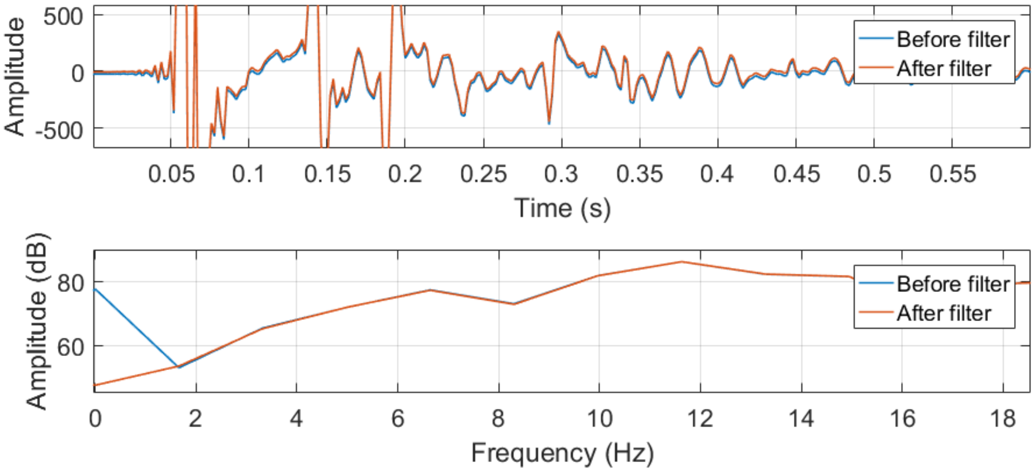

Figure 4.24: Example trace before (blue) and after (red) 2.5 Hz low-cut filter to eliminate DC shift.

Similarly to the Gabon test, clipped traces are not included in the inversion. Here, we have used receivers that are with offsets between 65 and 120 m, which correspond to departing angles for the direct wave of ~66-76° relative to vertical. The coordinates of the air guns and receivers that were used in the inversion are plotted in Figure 4.25, and the black circle shows the approximate area where receivers are overloaded within. The receivers will be numbered as indicated by the numbering in Figure 4.25 later in this section.

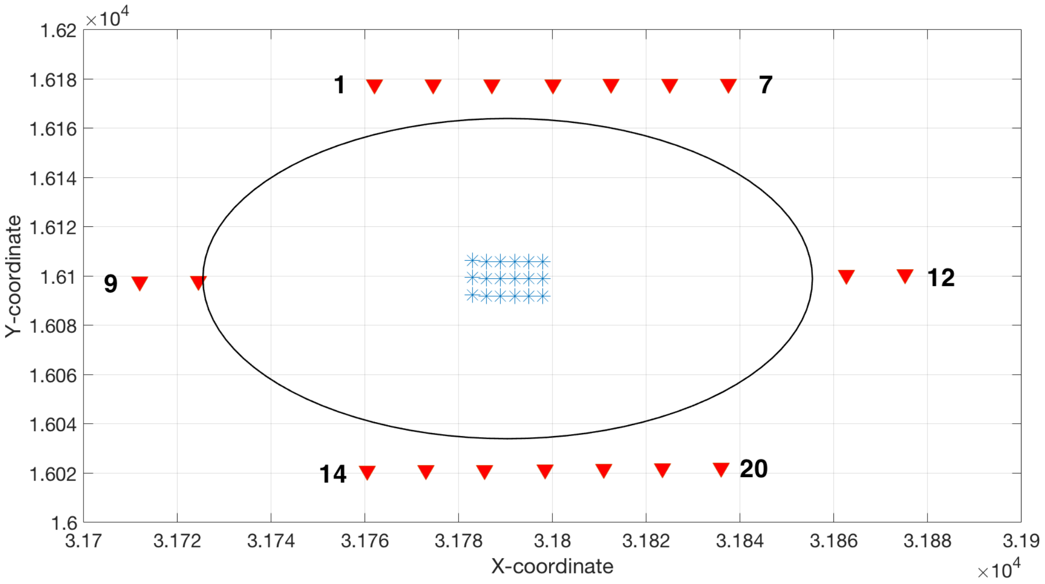

Figure 4.25: Coordinates for air guns (blue crosses) and receivers used in inversion (red triangles) from the Frigg-Gamma test. The minimum offset of 65 m is highlighted by the circle. The receivers are numbered as indicated for later plots in this section. Note that only 18 air guns are plotted here, because we assume that a cluster of two air guns can be described as one single air gun.

4.4.2 Inversion Results

The inversion was carried out for one shot with the receivers shown in Figure 4.25. Some of the details about the inversion are provided in Table 4.4.

Parameter	**Value**
Initial error [%]	60.1
Final error [%]	31.7
Iterations for first frequency window	10
Total number of iterations	18

Table 4.4: General information about inversion for shallow water data set.

We show the data from these receivers in Figure 4.26 (top), divided into three boxes corresponding to the three streamers included in the inversion. Also shown in Figure 4.26 are the estimated data after the inversion (middle) and residuals (bottom). The data in all three plots are multiplied by t to make the bubble and reflections more visible. Due to the shallow water, the water bottom reflection is recorded after about 150 ms. The receiver ghost is recorded about 50 ms later, which corresponds well with a streamer depth of about 35 meters. The water bottom reflection and the associated ghosts appear in the estimated data, because they are included in the forward operator as an attempt to make the algorithm more robust with respect to the reflections (as explained in Subsection 3.2.1). We can observe from the residuals that most of the energy that contribute to the residual error of 31.7% are high-frequency reflections and errors in the modeling of the primary peak and source ghost of the direct wave. For example, the first order multiple from the water bottom reflection, recorded at about 290 ms and highlighted by the blue arrow, is preserved in the residuals because the forward modeling does not attempt to model this event. Also evident from the residuals is that the water bottom reflection and the associated ghosts are not modeled accurately. For example, for trace number 1-7, the modeled water bottom reflection has higher amplitude than the recorded water bottom reflection. This can be due to the assumption of that the water bottom reflection is constant, while it in reality decreases with angle of incidence.

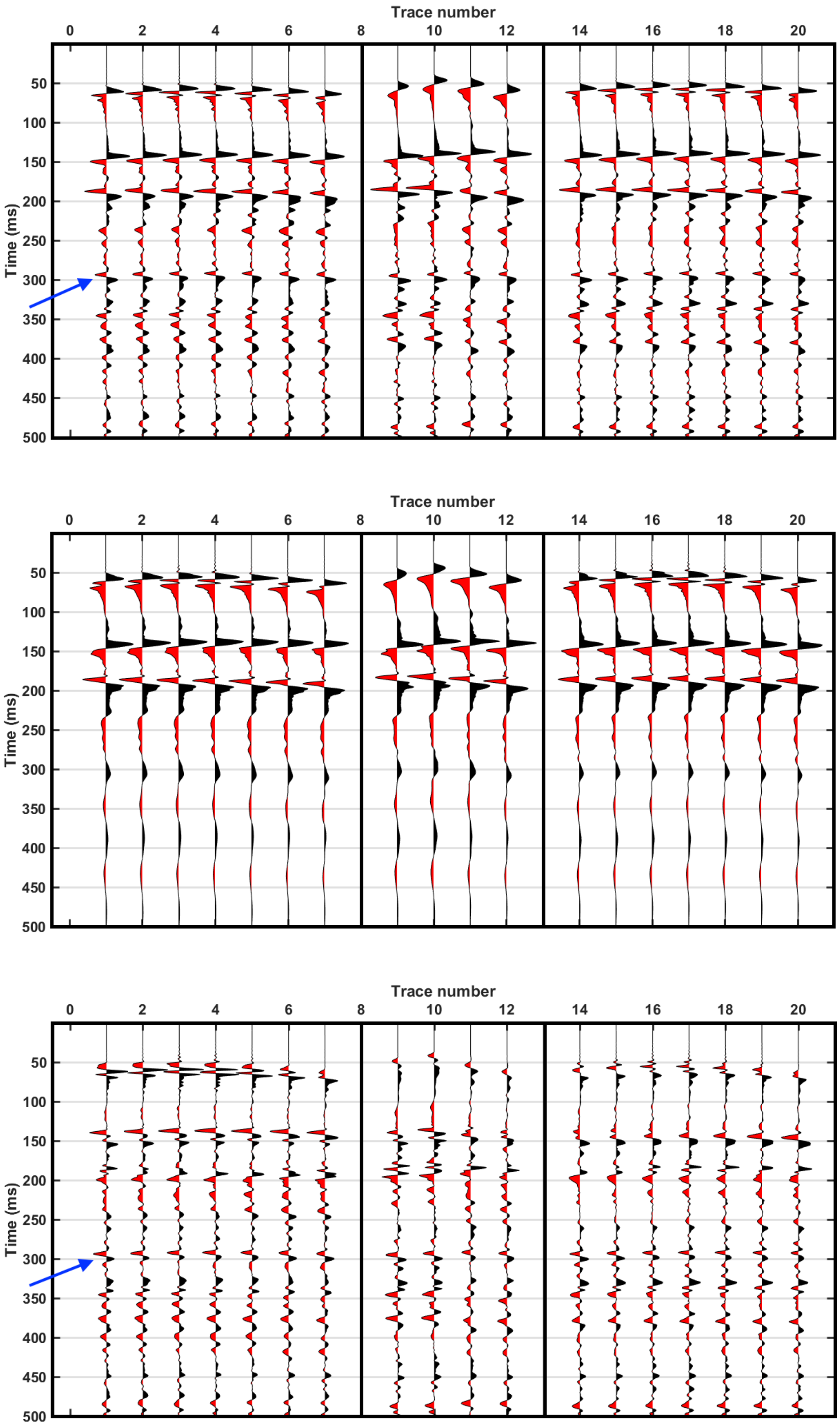

Figure 4.26: Top: Real data. Middle: Modeled data after inversion. Bottom: Difference. A t-gain is applied to the data to make the reflections and the bubble more visible. The relative error between the real data and the modeled direct wave from the initial model was 60.1%, while the error was 31.7% after the inversion. Each box correspond to receivers from one streamer. The blue arrows highlight the first order multiple of the water bottom reflection which is preserved in the residuals.

The relative error, trace by trace, is shown in Figure 4.27. Most of the minimization occurs for the traces 1-7. In Figure 4.28, we show the initial (red) and estimated (blue) model parameters for each air gun; α (top left), β_0 (top right), β_1 (bottom left) and firing time delay (bottom right). The initial values of the water depth and water bottom reflection coefficient were 119 m and 0.3, respectively, while the estimated values were 117.3 m and 0.46 after the inversion. The sea surface reflection coefficient was estimated to -0.9374. The initial and final streamer depth for the three streamers are shown in Figure 4.29. The streamer to the left in the figure show the largest deviations, where the largest error between the real and modeled primary peak and source ghost also is observed in Figure 4.26 and 4.27.

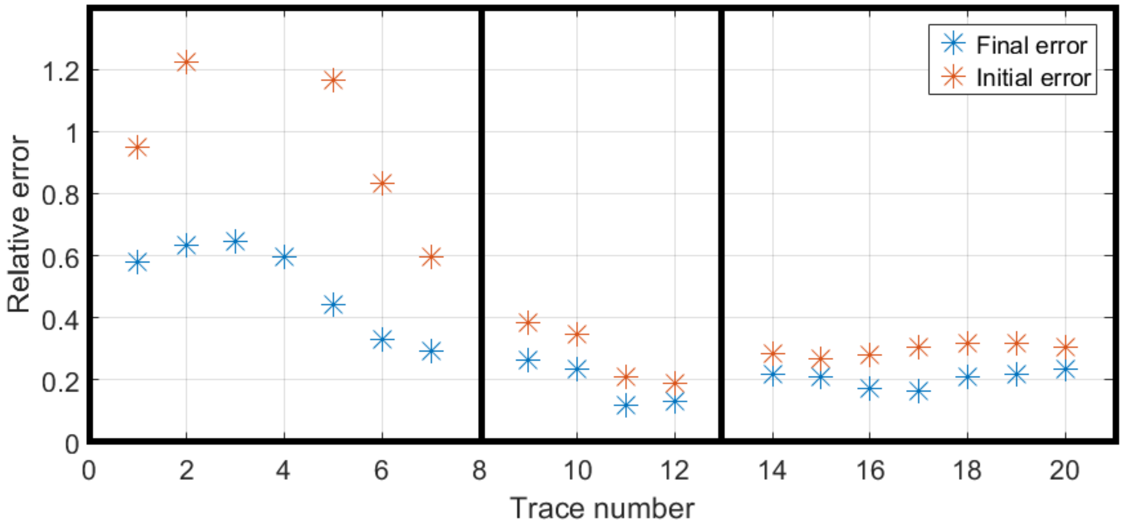

Figure 4.27: Initial (red) and final (blue) error, trace by trace. Most of the minimization occurs at receivers at high departing angles, due to the complexity of the wavelet from the dual-level source at these angles. Each box correspond to receivers from one streamer.

With the same approach as for the deepwater test, we model notional source signatures with the estimated α, β_0 and β_1-values. The notional source signatures are shown in Figure 4.30 (bottom), and compared with notional source signatures estimated from NFH-measurements (top). The residual ghost in the NFH-notionals is clearly present, as highlighted by the blue arrow. For notional number 11-13, the amplitude of the second bubble oscillation is significantly larger for the notional source signatures estimated from the inversion, highlighted by the red circle. We observe that the bubble time period for these air guns is 90-100 ms, which corresponds with the travel time difference between the direct wave and the water bottom reflection in the data in Figure 4.26.

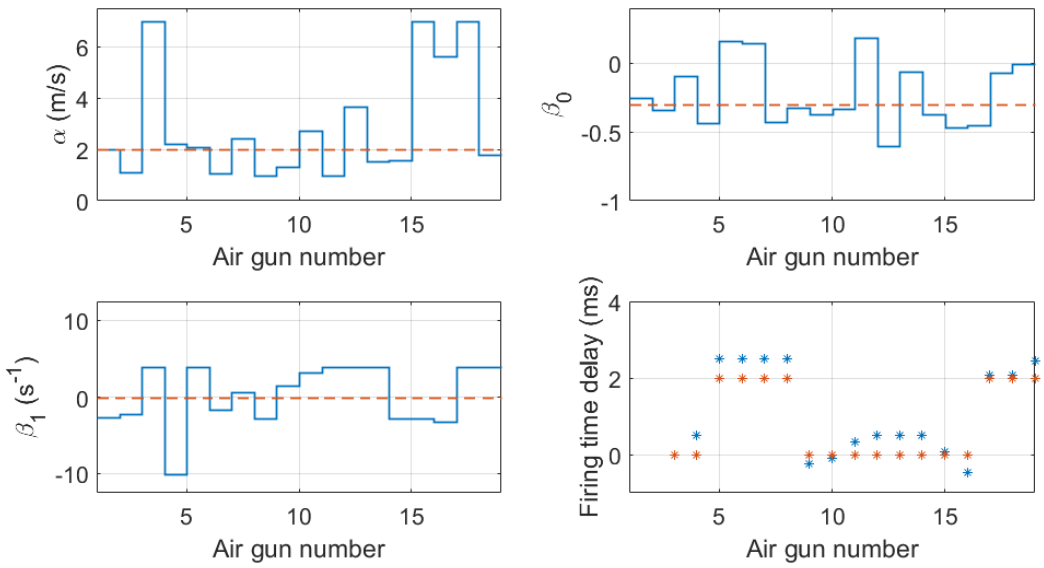

Figure 4.28: Initial (dashed red) and estimated (solid blue) model parameters after inversion. Top left: α, top right: β_0, bottom left: β_1 and bottom right: firing time delay.

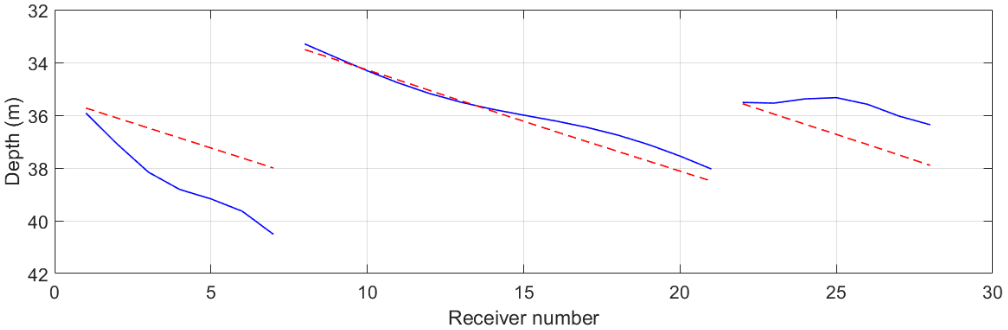

Figure 4.29: Initial (dashed red) and estimated (solid blue) streamer depth for each streamer. Receiver number 10-18 were not included in inversion. Note that the receivers are here numbered differently than in the other figures in this section.

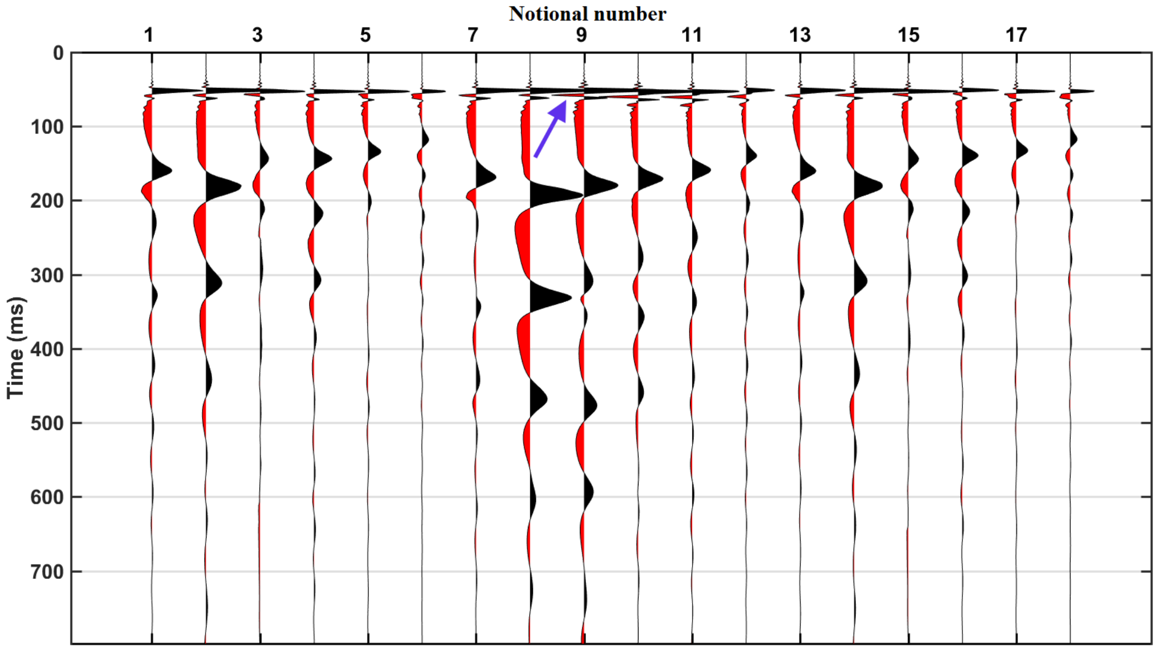

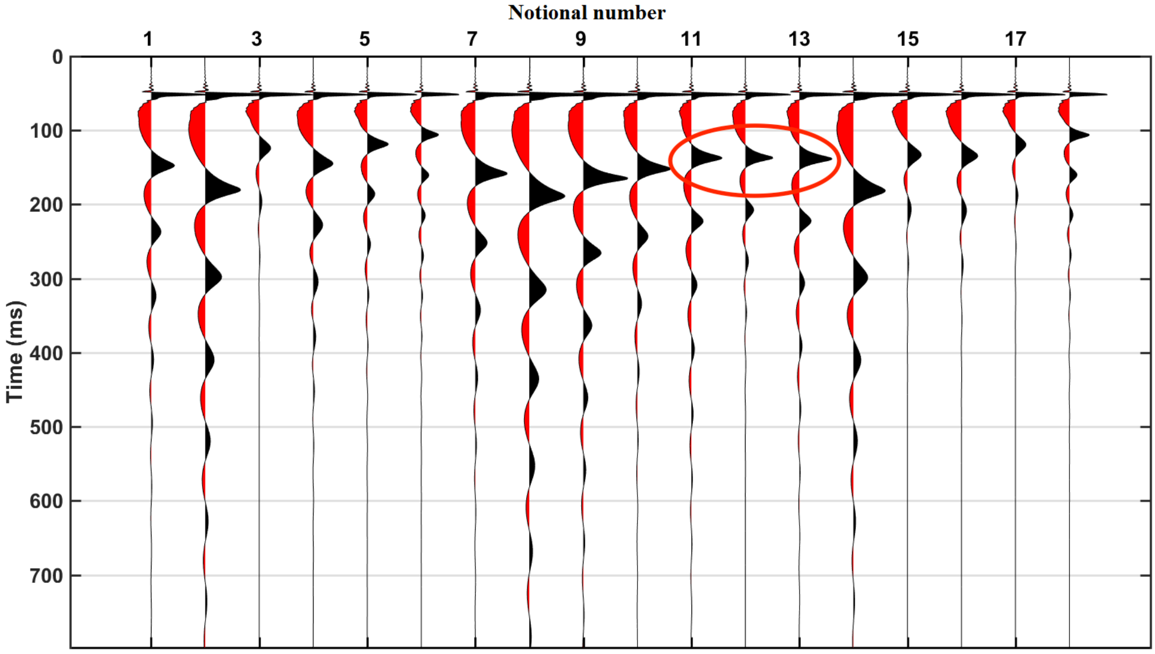

Figure 4.30: Top: Notional source signatures from near-field hydrophone measurements. Bottom: Notional source signatures estimated from the direct wave. Note that there are residual ghosts in the notionals from near-field hydrophones (highlighted by the blue arrow). We also observe that the amplitude of the second bubble oscillation is significantly larger for notional number 11-13 for the notional source signatures from the inversion, highlighted by the red circle.

The vertical far-field signatures from the notional source signatures from the inversion and from NFH-measurements are compared with a vertical far-field signature from the Nucleus software in Figure 4.31. The sea surface reflection coefficient is set to -1 for all the far-field signatures and the firing time delays are the same. The far-field signature from the inversion-method matches Nucleus well, whereas the far-field signature from the NFH-method is different due to the same reasons as in the deepwater test. With regards to the bubble, there are also significant dissimilarities, especially where highlighted by blue arrows. The estimated bubble with the notional source signatures from the inversion is very different around 0.1-0.15 s after the primary peak, which correspond to the travel time difference between the direct wave and the water bottom reflection and its ghosts in the real data. Clearly, the inversion is influenced by the strong reflections from the water bottom in the data, even if they are included in the forward modeling of the algorithm.

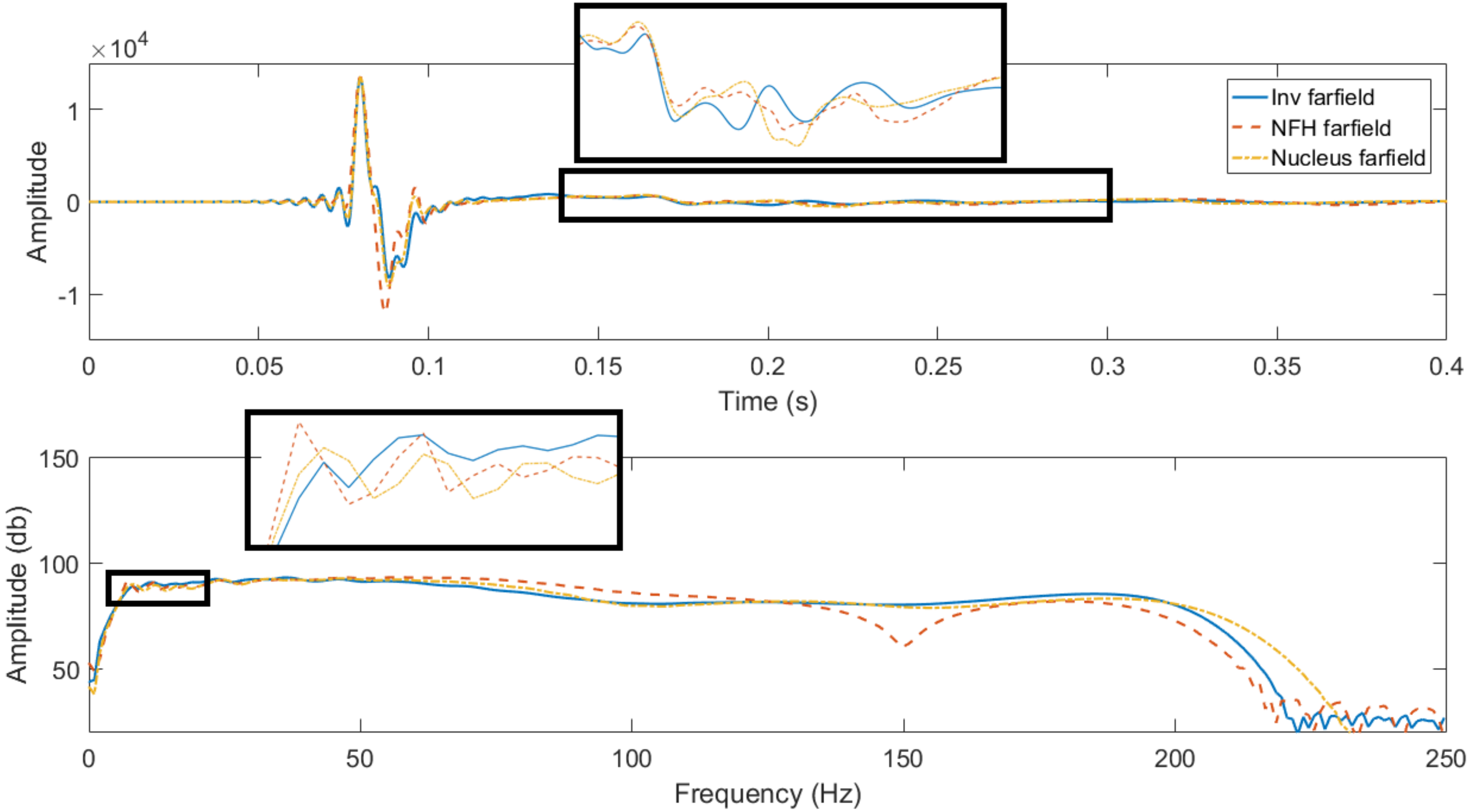

Figure 4.31: Top: Estimated vertical far-field signatures 5000 m below source array with notional source signatures from inversion (solid blue), from NFH-measurements (dashed red) and Nucleus signature (dashdotted yellow). Bottom: Corresponding frequency spectrum. The primary peak and source ghost from our method corresponds well with the far-field signature extracted from Nucleus, while the estimated peak and source ghost are inaccurate for the NFH-method, due to the residual ghost present in the notional source signatures. The zoom in the plots reveal the large differences in estimated bubble from the three methods, where the high amplitude bubble in the far-field from the inversion (highlighted by the blue arrows) is most likely due to that the inversion is influenced by reflections from the water bottom. NB: Note that the scale of the zoom is different from the scale of the full figure.

4.4.3 Source Designature Results

We use the estimated notional source signatures from the inversion and NFH-measurements in a designature flow, where the theory is explained in Section 3.4. The same assumptions as for the deepwater test are made when we estimate the departing angle for the water bottom reflection at each receiver, i.e. we assume that the water bottom is flat and that the velocity in the water layer is constant. The estimated sea surface reflection coefficient of -0.9374 is used when the source ghost is added to the far-field signature. The desired output wavelet is shown in Figure 4.32, in time- (left) and frequency-domain (right). The designature was unstable for frequencies above ~75 Hz, so the corner frequencies of the spectrum are 4,7, 70 and 100 Hz.

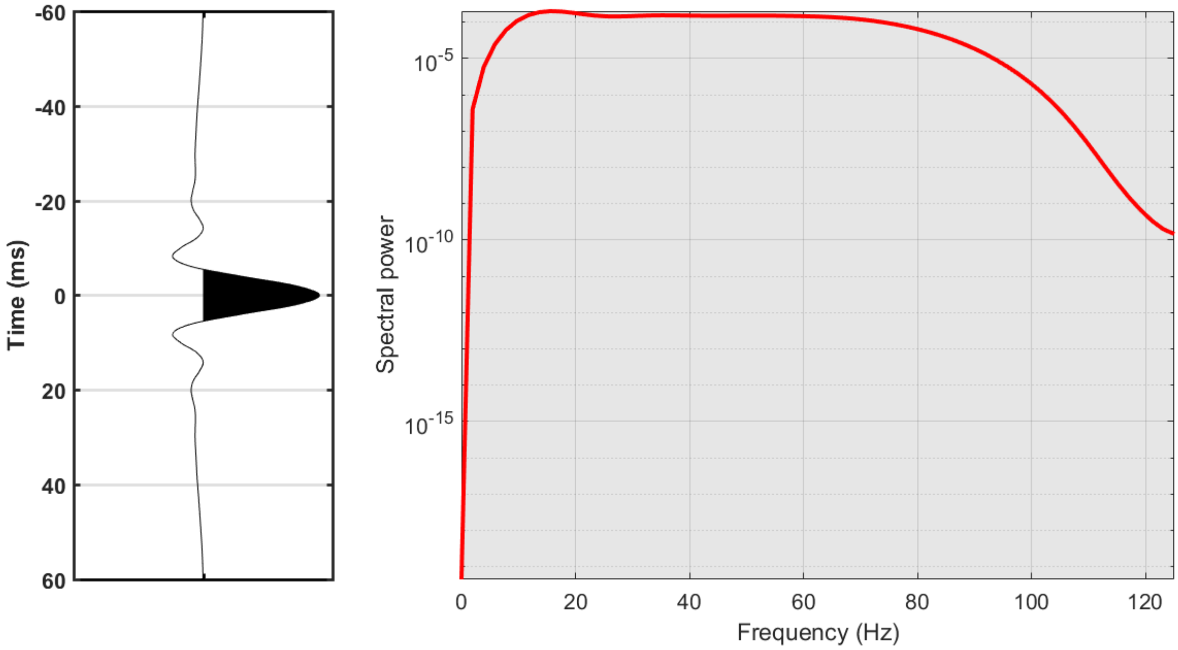

Figure 4.32: Desired wavelet for designature in time (left) and frequency domain (right). The corner frequencies of the spectrum are 4, 7, 70 and 100 Hz.

The designature was applied to 29 traces, along the streamer that was second closest to the source (there is no ringing in the traces from this streamer), as shown in Figure 4.33. The maximum offset for the traces that designature was applied to was 225 m, which corresponds to an incident angle of ~45° when the water depth is ~120 m. Assuming acoustic velocities of 1500 m/s in the water layer and 2000 m/s in the first layer below the water bottom, the critical angle is ~49°, so the water bottom reflection should be below critical angle for the traces included in the designature algorithm.

Figure 4.34 shows the input data in a common shot-gather (left) and the data after designa-

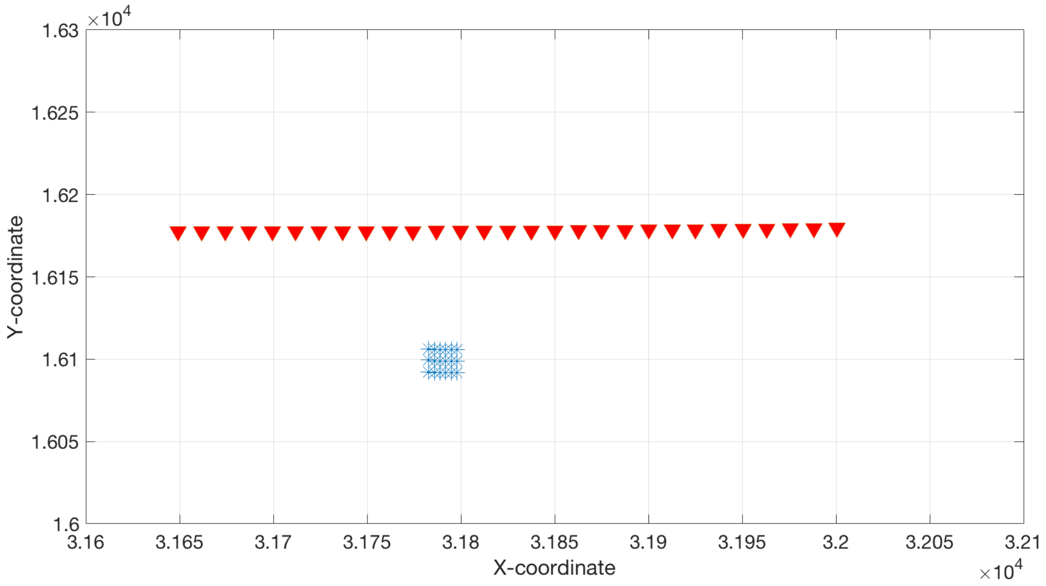

Figure 4.33: Map showing position of receivers (red triangles) included in designature flow relative to the air guns (blue crosses).

ture with the notional source signatures from the inversion (middle) and from NFH-measurements (right). The water bottom reflection is expected to be zero-phase after designature because the impedance difference between water and the muddy water bottom is typically significantly larger than impedance differences in the very shallow subsurface. This should yield a clear reflection from the water bottom, where tuning and interference with events from just below the water bottom is not significant.

The water bottom reflection appears to be relatively zero-phased after designature with both sets of notional source signatures. However, it seems to be more successful after designature with the notional source signatures from the inversion. The first order multiple of the water bottom (highlighted by the black arrow in the gather to the left) is also zero-phased, even though the departing angle of this event is different than for the primary reflection from the water bottom. Figure 4.35 shows the same gathers after aligning the water bottom; input (left), designature with notional source signatures from inversion (middle) and from NFH-measurements (right). It is difficult to see any clear difference between the designatured gathers with regards to the bubble. The receiver ghost is not a horizontal event for the same reason as in the deepwater test. Figure 4.36 shows a stack of the designatured traces with notional source signatures from the inversion (left), from NFH-measurements (middle) and the difference (right), where deeper reflections will stack out due to non-horizontal move-out after aligning the water bottom reflection. Hence, mostly energy from the water bottom reflection should appear in the stacked traces. The zero-phasing of the water bottom reflection, highlighted by the black arrow in the trace to the left, is successful with the notional source signatures from the inversion. The zero-phasing with NFH-notionals is inaccurate, due to the same reasons as for the deepwater test. With regards to the bubble, it is difficult to see large differences between the designature with the two sets of notional source signatures. However, we observe relatively high-frequency events (highlighted by the red circle) in the designature with the notional source signatures from the inversion between 250 and 350 ms, that are not present in the designature with NFH-notionals. This is possibly caused by the inaccurately estimated far-field signature from the notional source signatures from the inversion because of the influence of the water bottom reflection and its ghost, as seen in the vertical far-field signatures in Figure 4.31.

Based on the results, the designature with the notional source signatures from NFH-measurements appear to be more stable with regards to the debubbling when the notional source signatures are estimated from shallow water data sets.

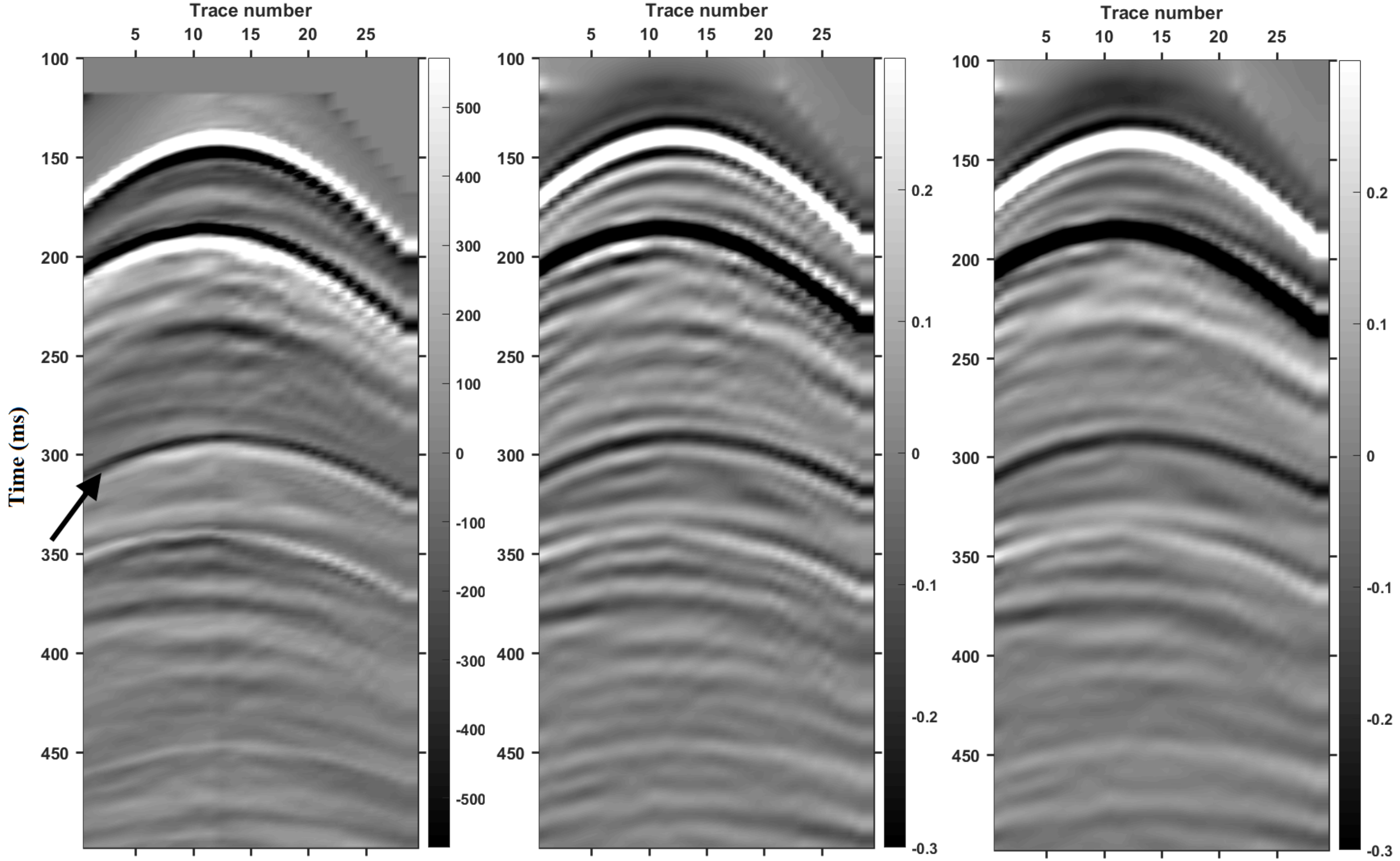

Figure 4.34: Results after designature. Left: Shot-gather prior to designature. Middle: After designature using notional source signatures from the inversion. Right: After designature with notional source signatures from NFH-measurements. The black arrow highlight the first order multiple of the water bottom, which is also zero-phased after designature with the two sets of notional source signatures.

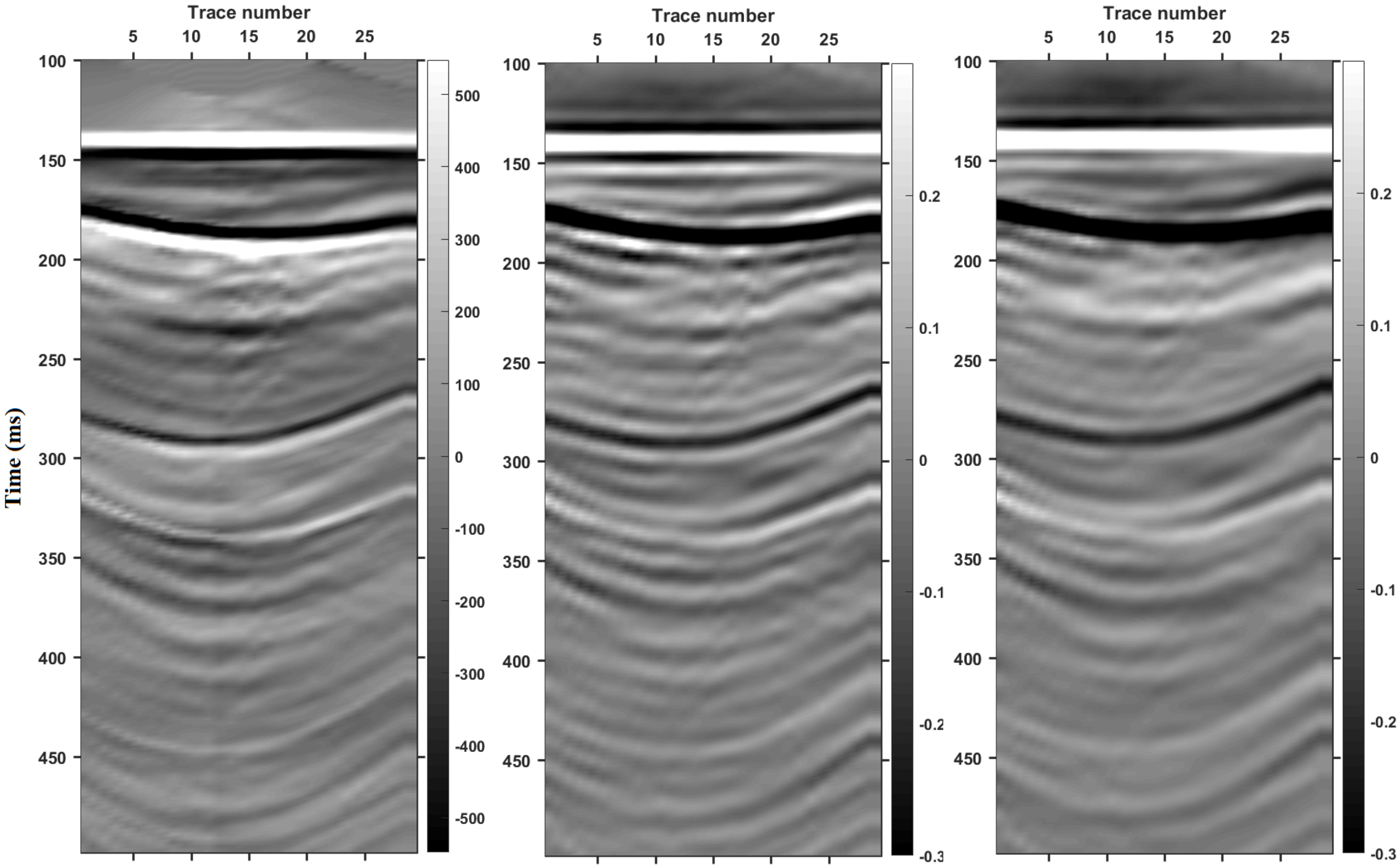

Figure 4.35: Results after aligning water bottom reflection. Left: Shot-gather prior to designature. Middle: After designature with notional source signatures from inversion. Right: After designature with notional source signatures from NFH-measurements. Deeper reflections have move-out upwards because aligning the WB reflection will over-correct the move-out of deeper reflections (with higher apparent velocity).

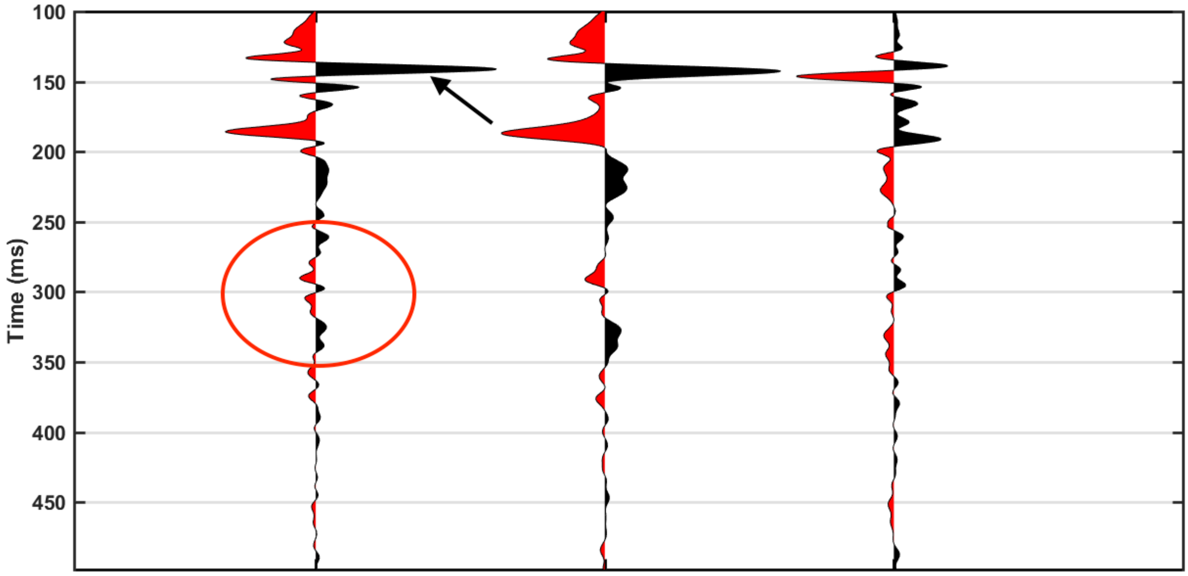

Figure 4.36: Left: Stack of the designatured traces with notional source signatures from inversion. Middle: Stack of the designatured traces with notional source signatures from NFH-measurements. Right: Difference. The red circle highlight high-frequency events that appear in the designature with notional source signatures from the inversion. The water bottom reflection, highlighted by the black arrow, is better zero-phased with the notional source signatures from the inversion due to better estimation of the primary peak and source ghost in the far-field signature. The receiver ghost stacks out due to the variable-depth streamer profile used during acquisition.

Chapter 5

Discussion

We have in this thesis presented an inversion algorithm that takes advantage of the recordings of the direct wave in source-over-spread acquired seismic data to estimate source signatures. A common method for source signature estimation today is to use near-field hydrophones. However, as discussed earlier, this approach can be unstable for dense air gun arrays, which is clearly evident from the residual ghosts in the notional source signatures from NFH-measurements presented in this thesis. The alternative approach of using mid-field measurements can overcome this challenge, but has other limitations, as apparent from the results presented in the thesis.

For the test on the deepwater data set, the estimated direct wave from the inversion appeared to be more accurate than from notional source signatures from NFH-measurements for the first part of the bubble, when compared with the real direct wave recorded at the streamers. However, for the later part, where the bubble is weaker, the estimated direct wave from the NFH-measurements was more accurate. We see four possible reasons for this:

1. The optimization of the inversion algorithm will focus more on minimizing the difference between the real and modeled direct wave where the amplitude is strongest, i.e. for the first part of the bubble.
2. We expect less non-linear interaction between the bubbles when they are weaker, which makes it easier to remove the effect of the neighbouring bubbles from the NFH-measurements.
3. The inversion relies on an accurate forward modeling. The modeling of the bubbles will be increasingly inaccurate with time, and therefore, the modeling is not able to recreate the source signature for the weaker part of the bubble.

4. The search algorithm can be trapped in a local minimum, which restricts the modeling of the later part of the bubble.

One approach to cope with the third problem can be to include more model parameters (more degrees of freedom) to model the air bubbles. When the notional source signatures were tested in a designature flow, the inversion method appeared to zero-phase the bubble better. Based on the results, the inversion approach seems to estimate the strongest part of the bubble more accurately, while the NFH-approach is better for the weaker part. Hence, a hybrid between the two methods can be appropriate to exploit the complimentary advantages which can provide more precise estimation of the full bubble pulse than what is achievable today.

For the test on the shallow water data set, the water bottom reflection and its receiver ghost influenced the stability of the inversion, even when included in the forward modeling of the inversion algorithm as an attempt to avoid this problem. One of the advantages of near-field hydrophones is that the recorded direct wave will have a significantly stronger amplitude than the water bottom reflection, even in shallow water depths. For mid-field measurements, the reflections will be less negligible in shallow water. To illustrate this, we consider an example where an air gun is placed at 6 m depth, and the direct wave is recorded in a NFH placed 1 m above the air gun and in a streamer towed 30 m below the air gun. Given a water depth of 100 m and a water bottom reflection coefficient of 0.3, we expect the direct wave recorded in the near-field hydrophones to be ~630 times stronger than the water bottom reflection and ~18 times stronger in the deep-towed streamer at zero-offset. With a PBR of 20 (which is low for modern air gun arrays), the bubble of the direct wave will be ~30 and ~1 times stronger than the water bottom reflection. However, the departing angle of the direct wave and the water bottom reflection will be different for non-zero offset. Hence, the amplitude difference between the two will decrease with offset because of source ghost tuning and source directivity. Therefore, the water bottom reflection will not be negligible for larger offsets in the inversion algorithm, as evident in the test on the shallow water data set. Most of the near-offset traces could not be included in the inversion, as the overloading of the receiver system damaged the recordings of the bubble of the direct wave in these traces. Landrø et al. (1994) did not have clipped traces in the acquired data, and the inversion was robust with respect to the water bottom reflection (in similar water depths as for the shallow data set tested in this thesis, but the mini-streamer was towed closer to the source than in source-over-spread acquisition and the PBR was probably lower than in modern air gun arrays). Hence, the inversion algorithm presented here is likely to perform better in shallow water if there is no late effect because of the overloading of the receiver system. We also observe that the inversion is robust with respect to the first order multiple of the water bottom reflection (recorded at about 300 ms, corresponding to a water depth of approximately 220 m given the offset between the source and the receiver), even if it is not included in the forward modeling of the algorithm. This indicates that the algorithm can perform well in water depths of this level, even if clipped traces cannot be included in the inversion.

The estimated primary peak and source ghost of the far-field was very different for the two methods. This affects the zero-phasing of the water bottom reflection when the notional source signatures were used in the designature flow. The notional source signatures from the inversion performed significantly better, because the primary peak and source ghost of the estimated far-field signature with notional source signatures from NFH-measurements were inaccurate due to the residual ghost in the notional source signatures. However, the zero-phasing is expected to be more successful when notional source signatures from NFH-measurements are used in more robust designature algorithms, so we do not regard this as a significant advantage of the inversion approach. When the far-field is estimated from the two methods, we also assume that the far-field is a shifted and scaled version of the primary peak, even though this is not likely to be accurate. Hampson (2017) suggest to estimate both notionals and ghost notionals to take into account that the reflection of the sea-surface on the source-side is more complex than what we typically assume. We can describe the physics of the source-side reflection more accurately by e.g. taking into account that the sea-surface reflection coefficient is frequency- and angle-dependent (Orji et al., 2013).

Already mentioned as one of the disadvantages of estimating source signatures from mid-field measurements is that the receivers are placed further away from the source array and closer to the water bottom, which makes the approach more prone to interference with subsurface reflections. Additionally, the receiver positions are needed in the forward modeling, but they are not accurately known in practice. This affected the optimization of the inversion with regards to the primary peak and source ghost of the receivers, but it is not expected to affect the estimation of the bubble significantly, due to its low-frequency content. In the proposed algorithm here, we treat the depth of the streamers as unknown parameters. However, lateral positions of the receivers in source-over-spread acquisition are not expected to be known accurately either, and could therefore be included as unknown model parameters in the inversion. The inaccuracy of the receiver positions also influenced the stability of the firing time delay as unknown model parameters. The intention of including the firing time delays as unknown model parameters is to correct for the errors in the triggering time of each air gun relative to the others. However, as the receiver positions are inaccurate, the firing time delays attempt to correct for the difference in real and modeled travel time between the source and each receiver. Typically, the uncertainty in firing time can be up to approximately 1 ms, which corresponds to an error in source-receiver distance of 1.5 m (assuming water velocity of 1500 m/s). If the error in source-receiver distance is significantly larger than this, the firing time delay will be more sensitive to errors in source-receiver distance than the relative difference in firing time between the air guns.

With regards to the forward modeling of the algorithm, there are also disadvantages, because inversion algorithms rely on an accurate forward operator to achieve good results. As Ziolkowski and Johnston (1997) write about Landrø and Sollie (1992) (where they present their inversion approach to estimate source signatures from mini-streamer data);

> "*The method is entitled "Source-signature estimation by inversion", but it is really source-signature estimation by iterative forward modeling: the accuracy of the solution is limited not only by the the precision with which the geometry and hydrophone sensitivities are known, it is also constrained by the precision with which the forward model is able to generate the true wavefield.*"

In other words, the results from the inversion are restricted by the source signature modeling. This is evident from the deepwater data set, where the forward operator can be improved to model the direct wave more accurately. By adding more model parameters (i.e. degrees of freedom), we might be able to model the bubble more precisely. In theory, we can include so many model parameters to describe the air bubbles from each gun that the inversion algorithm acts more like a curve fitting algorithm. However, this can affect the accuracy when source signatures are extrapolated to directions that are not constrained by the data, for example to vertical far-field signatures. Additionally, by including many unknown model parameters, we will make the algorithm more prone to noise.

Due to the late effect of the overloading of the receivers at near offsets, we only use receivers where the departing angle of the direct wave is ~65-75° relative to vertical. Hence, we assume that the notional source signatures we estimate from the direct wave at relatively high departing angles are representative the far-field signature around vertical direction. This thesis has not provided an in-depth study on this matter, but this can be done by e.g. comparing the angle-directivity of difference between the estimated far-field signature from Nucleus with far-field signatures from the notional source signatures from the inversion. If the difference is very large around the vertical compared to at higher angles, this might indicate that the notional source signatures from the inversion do not describe the far-field signature in the vertical direction very accurately. However, the designature results imply that the extrapolation of source signatures to low departing angles is successful.

The algorithm also rely on modeling of the release of air from the air gun chamber to obtain reasonable PBR-ratios. We have solved this by scaling the primary peak of each notional source signature, but this approach does not model the shape of the primary pulse correctly. Landrø et al. (1994) model the actual transfer of air from the air gun chamber, which is a more accurate approach. The shape of the primary pulse is expected to be well determined for notional source signatures from NFH-measurements because the near-field hydrophones measure the actual primary peak and this part of the measurement is not contaminated by contributions from the other air guns (and their ghosts). We did not experience any problems with our approach of scaling the primary peaks in the designature flow, but other designature algorithms might be more sensitive to this.

In this thesis, we have only studied the value of source signature estimation for the designature step in seismic processing. The designature was designated for the water bottom reflection, where the departing angle can be calculated given a few assumptions. However, for deeper reflections, more assumptions are needed to estimate the departing angle, and it is therefore significant uncertainty related to how precisely the departing angle can be calculated. Hence, the quality of the designature may be limited by the assumptions that are needed for designature of deeper reflections, not the accuracy of the source signature itself. Accurate source signatures are of importance in SRME, time-lapse, AVO and FWI, among others. The low-frequency part of the source signature is especially important for FWI, and therefore, better bubble estimation can yield uplift in results within this area. Finally, it is important to stress that the recorded direct wave in source-over-spread seismic data does not only provide knowledge about the source signature, but can also be utilized to for example estimate an angle- and frequency-dependent sea surface reflection coefficient and correct source and receiver positions, as has earlier been done from near-field hydrophone measurements (Kryvohuz and Campman, 2016) or dual-sensor technology (Orji et al., 2013).

Chapter 6

Conclusions

We have presented an inversion algorithm to estimate source signatures based on the recordings of the direct wave in deep-towed streamers below the source. The thesis can provide a foundation for further work with regards to new possibilities for source signature estimation that arise from source-over-spread acquired seismic data. A few key conclusions can be stated:

- The proposed algorithm performs well for data sets acquired in deep water and can provide more accurate estimation of source signatures, especially for the strongest part of the bubble.
- The algorithm can be further improved to estimate the bubble better by including more model parameters to describe the bubbles from each air gun.
- For shallow water data sets, the algorithm is sensitive to reflections from the water bottom, mainly because near-offset traces were damaged. Accurate recordings of the bubble of the direct wave at near-offsets will yield a more robust inversion in shallow water.
- Measurements of the direct wave in source-over-spread seismic data do not only provide value for source signature estimation, but should also be utilized to estimate sea surface reflection coefficients and correct source and receiver geometries.

Bibliography

Amundsen, L., Landrø, M., 2016. Broadband seismic technology and beyond Part VII: CGG's BroadSeis - a change of thinking. Geo ExPro 10 (5).

Backus, G., Gilbert, F., 1968. The resolving power of gross earth data. Geophysical Journal International 16 (2), 169–205.

Backus, G., Gilbert, F., 1970. Uniqueness in the inversion of inaccurate gross earth data. Philosophical Transactions of the Royal Society of London A: Mathematical, Physical and Engineering Sciences 266 (1173), 123–192.

Backus, G. E., Gilbert, J., 1967. Numerical applications of a formalism for geophysical inverse problems. Geophysical Journal International 13 (1-3), 247–276.

Barker, D., Landrø, M., 2012. Simple expression for the bubble-time period of two clustered air guns. Geophysics 77 (1), A1–A3.

Bunks, C., Saleck, F. M., Zaleski, S., Chavent, G., 1995. Multiscale seismic waveform inversion. Geophysics 60 (05), 1457–1473.

Claerbout, J., 1986. Fundamentals of geophysical data processing. Geophys. J. Roy. Astron. Soc 86 (1), 217–219.

Davidson, C., Poole, G., 2015. Far-field source signature reconstruction using direct arrival data. In: 77th EAGE Conference and Exhibition 2015.

Flynn, H., 1964. Physics of acoustic cavitation in liquids. Physical acoustics 1 (Part B), 57–172.

Gilmore, F. R., 1952. The growth or collapse of a spherical bubble in a viscous compressible liquid.

Haavik, K. E., Landrø, M., 2015. Variable source depth acquisition for improved marine broadband seismic data. Geophysics 80 (3), A69–A73.

Hampson, G., 2017. Notional ghosts. In: 79th EAGE Conference and Exhibition 2017.

Helgebostad, K. S., 2016. Source signature estimation based on recordings in deep-towed streamers below the source. TPG4570: Specialization Project, NTNU.

Helgesen, J., Landrø, M., 1993. Estimation of elastic parameters from AVO effects in the τ-p domain. Geophys. Prosp. 41 (03), 341–366.

Herring, C., 1941. Theory of the pulsations of the gas bubble produced by an underwater explosion.

Hill, D., Combee, C., Bacon, J., 2006. Over/under acquisition and data processing: The next quantum leap in seismic technology? First Break 24 (6).

Hopperstad, J., Laws, R., 2006. Source signature estimation-attenuation of the seafloor reflection error in shallow water. In: 68th EAGE Conference and Exhibition incorporating SPE EUROPEC 2006.

Johnson, D. T., 1994. Understanding air-gun bubble behavior. Geophysics 59 (11), 1729–1734.

Keller, J. B., Kolodner, I. I., 1956. Damping of underwater explosion bubble oscillations. Journal of applied physics 27 (10), 1152–1161.

Kirkwood, J., Bethe, H., 1942. OSRD report no. 588.

Kryvohuz, M., Campman, X., 2016. Optimization of sea surface reflection coefficient and source geometry in conventional dual source flip/flop marine seismic acquisition. In: SEG Technical Program Expanded Abstracts 2016. Society of Exploration Geophysicists, pp. 188–192.

Landrø, M., 2000. Source signature determination by inversion of ministreamer data. The Leading Edge 19 (01), 46–49.

Landrø, M., Amundsen, L., 2010. Marine seismic sources Part I. Geo ExPro 7 (1).

Landrø, M., Amundsen, L., Barker, D., 2011. High-frequency signals from air-gun arrays. Geophysics 76 (4), Q19–Q27.

Landrø, M., Langhammer, J., Sollie, R., Amundsen, L., Berg, E., 1994. Source signature determination from ministreamer data. Geophysics 59 (8), 1261–1269.

Landrø, M., Sollie, R., 1992. Source signature determination by inversion. Geophysics 57 (12), 1633–1640.

Landrø, M., Strandenes, S., Vaage, S., 1991. Use of near-field measurements to compute far-field marine source signatures - Evaluation of the method. First Break 09 (08), 375–385.

Langhammer, J., 1994. Experimental studies of energy loss mechanisms in air-gun bubble dynamics. PhD thesis, NTNU.

Laws, R., Landrø, M., Amundsen, L., 1998. An experimental comparison of three direct methods of marine source signature estimation. Geophysical prospecting 46 (4), 353–389.

Lu, S., Whitmore, D. N., Valenciano, A. A., Chemingui, N., 2015. Separated-wavefield imaging using primary and multiple energy. The Leading Edge 34 (7), 770–778.

Marquardt, D. W., 1963. An algorithm for least-squares estimation of nonlinear parameters. Journal of the Society for Industrial and Applied Mathematics 11 (2), 431–441.

Moldoveanu, N., Seymour, N., Manen, D., Caprioli, P., 2012. Broadband seismic methods for towed-streamer acquisition. In: 74th EAGE Conference and Exhibition incorporating EUROPEC 2012.

Oldenburg, D. W., Li, Y., 2005. Inversion for applied geophysics: A tutorial. Near-surface geophysics: SEG, 89–150.

Orji, O. C., Sollner, W., Gelius, L. J., 2013. Sea surface reflection coefficient estimation. In: SEG Technical Program Expanded Abstracts 2013. Society of Exploration Geophysicists, pp. 51–55.

Parkes, G., Hatton, L., 2013. The marine seismic source. Vol. 4. Springer Science & Business Media.

Parkes, G., Hegna, S., et al., 2011. A marine seismic acquisition system that provides a full 'ghost-free' solution. In: 2011 SEG Annual Meeting. Society of Exploration Geophysicists.

PlaneteEnergies, 2015. Offshore Oil and Gas Production. `http://www.planete-energies.com/en/medias/close/offshore-oil-and-gas-production`, [Online; accessed 26-May-2017].

Poole, G., Cooper, J., King, S., Wang, P., 2015. 3d source designature using source-receiver symmetry in the shot τ-p_x-p_y domain. In: 77th EAGE Conference and Exhibition 2015.

Ray, C. H., Moore, N. A., Oct. 5 1982. High resolution, marine seismic stratigraphic system. US Patent 4,353,121.

Rayleigh, L., 1917. VIII. On the pressure developed in a liquid during the collapse of a spherical cavity. The London, Edinburgh, and Dublin Philosophical Magazine and Journal of Science 34 (200), 94–98.

Schneider, W., Backus, M., 1964. Ocean-bottom seismic measurements off the california coast. Journal of Geophysical Research 69 (6), 1135–1143.

Siliqi, R., Payen, T., Sablon, R., Desrues, K., et al., 2013. Synchronized multi-level source, a robust broadband marine solution. In: 2013 SEG Annual Meeting. Society of Exploration Geophysicists.

Sønneland, L., Berg, E., 1985. A new method for separating wave fields into up-and down-going components. abstract b-46. In: 47th Meeting, European Association of Exploration Geophysicists, Extended Abstract.

Soubaras, R., Dowle, R., 2010. Variable-depth streamer–a broadband marine solution. First Break 28 (12).

Strandenes, S., Vaage, S., 1992. Signatures from clustered airguns. First Break 10 (8), 305–312.

Tait, P., 1888. The voyage of HMS challenger, vol. 2. London: Her Majesty's Stationary Office.

Tarantola, A., 2005. Inverse problem theory and methods for model parameter estimation. SIAM.

Ten Kroode, F., Bergler, S., Corsten, C., de Maag, J. W., Strijbos, F., Tijhof, H., 2013. Broadband seismic data—the importance of low frequencies. Geophysics 78 (2), WA3–WA14.

Tenghamn, R., Vaage, S., Borresen, C., et al., 2007. A dual-sensor, towed marine streamer; its viable implementation and initial results. In: 2007 SEG Annual Meeting. Society of Exploration Geophysicists.

Tikhonov, A. N., Arsenin, V. I., John, F., 1977. Solutions of ill-posed problems. Vol. 14. Winston Washington, DC.

Vinje, V., Lie, J. E., Danielsen, V., Dhelie, P. E., Silliqi, R., Nilsen, C.-I., Hicks, E., Camerer, A., 2017. Shooting over the seismic spread. First Break 35 (6), 97–104.

Ziolkowski, A., 1970. A method for calculating the output pressure waveform from an air gun. Geophysical Journal International 21 (2), 137–161.

Ziolkowski, A., Johnston, R., 1997. Marine seismic sources: Qc of wavefield computation from near-field pressure measurements. Geophysical prospecting 45 (4), 611–639.

Ziolkowski, A., Parkes, G., Hatton, L., Haugland, T., 1982. The signature of an air-gun array - Computation from near-field measurements including interactions. Geophysics 47 (10), 1413–1421.